Article

Cell Reports

Hyperexcitable Neurons Enable Precise and Persistent Information Encoding in the Superficial Retrosplenial Cortex

Graphical Abstract

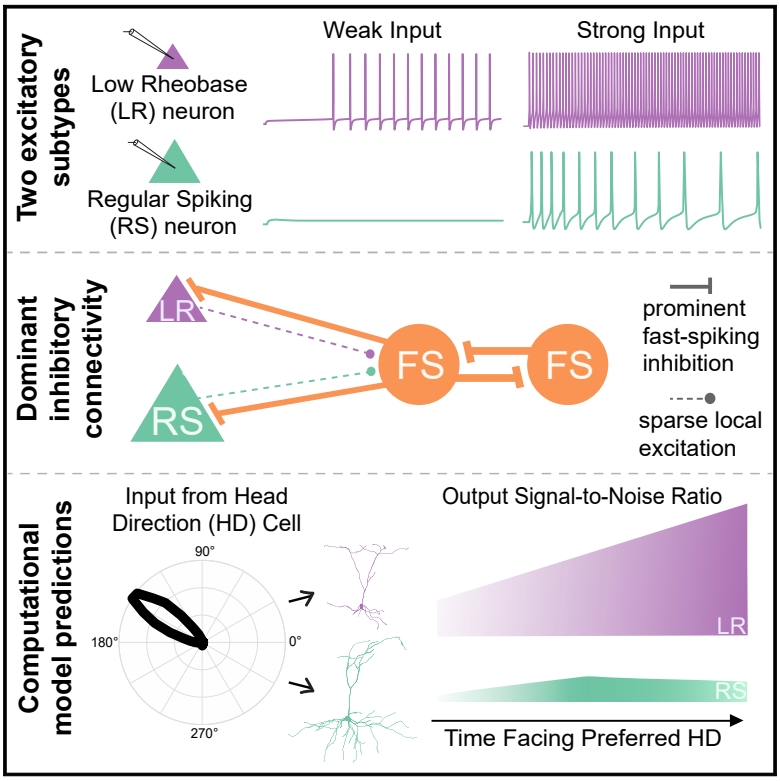

Authors

Ellen K.W. Brennan, Shyam Kumar Sudhakar, Izabela Jedrasiak-Cape, Tibin T. John, Omar J. Ahmed

Correspondence

ojahmed@umich.edu

In Brief

The retrosplenial cortex is critical for navigation and memory, but the underlying neural codes remain unclear. Here, Brennan et al. identify a distinct, prominent excitatory neuron whose intrinsic properties enable sustained encoding of head direction inputs. Their neuronal connectivity map reveals a retrosplenial circuit dominated by feedforward, not feedback, inhibition.

Highlights

- Two distinct subtypes of excitatory neurons in superficial retrosplenial cortex (RSC)
- Most common neuron in layer 2/3 of RSC is excitatory low-rheobase (LR) neuron
- LR intrinsic properties enable precise, sustained encoding of information
- Layer 2/3 of RSC is dominated by feedforward, not feedback, inhibition

Brennan et al., 2020, Cell Reports *30*, 1598–1612
February 4, 2020
https://doi.org/10.1016/j.celrep.2019.12.093

CellPress

OPEN ACCESS
CellPress

Cell Reports
Article

Hyperexcitable Neurons Enable Precise and Persistent Information Encoding in the Superficial Retrosplenial Cortex

Ellen K.W. Brennan,[1,2,6] Shyam Kumar Sudhakar,[1,6] Izabela Jedrasiak-Cape,[1] Tibin T. John,[1,2] and Omar J. Ahmed[1,2,3,4,5,7,*]

[1]Department of Psychology, University of Michigan, Ann Arbor, MI 48109, USA
[2]Neuroscience Graduate Program, University of Michigan, Ann Arbor, MI 48109, USA
[3]Michigan Center for Integrative Research in Critical Care, University of Michigan, Ann Arbor, MI 48109, USA
[4]Kresge Hearing Research Institute, University of Michigan, Ann Arbor, MI 48109, USA
[5]Department of Biomedical Engineering, University of Michigan, Ann Arbor, MI 48109, USA
[6]These authors contributed equally
[7]Lead Contact
*Correspondence: ojahmed@umich.edu
https://doi.org/10.1016/j.celrep.2019.12.093

SUMMARY

The retrosplenial cortex (RSC) is essential for memory and navigation, but the neural codes underlying these functions remain largely unknown. Here, we show that the most prominent cell type in layers 2/3 (L2/3) of the mouse granular RSC is a hyperexcitable, small pyramidal cell. These cells have a low rheobase (LR), high input resistance, lack of spike frequency adaptation, and spike widths intermediate to those of neighboring fast-spiking (FS) inhibitory neurons and regular-spiking (RS) excitatory neurons. LR cells are excitatory but rarely synapse onto neighboring neurons. Instead, L2/3 is a feedforward, not feedback, inhibition-dominated network with dense connectivity between FS cells and from FS to LR neurons. Biophysical models of LR but not RS cells precisely and continuously encode sustained input from afferent postsubicular head-direction cells. Thus, the distinct intrinsic properties of LR neurons can support both the precision and persistence necessary to encode information over multiple timescales in the RSC.

INTRODUCTION

The retrosplenial cortex (RSC) plays a critical role in learning and memory. In humans, damage to the RSC results in both anterograde and retrograde amnesia, often purging several years of recent memories (Ironside and Guttmacher, 1929; Heilman and Sypert, 1977; Valenstein et al., 1987; Todd and Bucci, 2015; Chrastil, 2018). Similar impacts on both anterograde and retrograde memory are seen in monkeys when the RSC is lesioned (Buckley and Mitchell, 2016). In rodents, RSC lesions impair performance on spatial learning and fear conditioning tasks (Vann et al., 2003, 2009; Van Groen et al., 2004; Keene and Bucci, 2008; Katche et al., 2013; Todd et al., 2015, 2017; Sigwald et al., 2016; Yamawaki et al., 2019b). Recent imaging studies in mice confirm that RSC neurons can display evidence of long-duration, persistent spatial memory engrams (Czajkowski et al., 2014; Milczarek et al., 2018; de Sousa et al., 2019; Hattori et al., 2019).

The RSC is also critical for spatial navigation (Maguire, 2001; Epstein, 2008). Human case studies show that RSC damage leads to disorientation in space in addition to memory impairments (Bottini et al., 1990; Takahashi et al., 1997; Ino et al., 2007; Osawa et al., 2007). Such patients can identify known scenes or locations but are unable to extract any orientation information from them and, thus, experience difficulties navigating even familiar environments (Bottini et al., 1990; Takahashi et al., 1997; Ino et al., 2007). A neuroimaging study identified the coding of head direction (HD) information in the RSC while participants navigated a novel virtual environment, suggesting that visual cues of orientation are processed, in part, by the RSC during navigation (Shine et al., 2016). Animal studies also report encoding of spatial information within the RSC, including that of HD, position, and turning behavior (Cho and Sharp, 2001; Alexander and Nitz, 2015; Vedder et al., 2016; Mao et al., 2017, 2018; Miller et al., 2019).

How is the RSC uniquely suited to carry out these spatial memory and navigation computations? This is a fundamental but unsolved circuit input-output transformation problem. The RSC receives prominent spatial and memory-related inputs from the hippocampus, subicular complex, anterior thalamus, secondary motor cortex, and visual cortex, as well as the contralateral RSC (Van Groen and Wyss, 1990, 2003; Wyss and Van Groen, 1992; Miyashita and Rockland, 2007). Recent studies have started to document the functional nature of these inputs to the RSC (Yamawaki et al., 2016, 2019a, 2019b; Sempere-Ferràndez et al., 2018; Sempere-Ferràndez et al., 2019). However, the precise properties of the RSC neuronal subtypes involved (Wyss et al., 1990; Sugar et al., 2011; Kurotani et al., 2013) are rarely studied in mice, and the local connectivity between RSC subtypes is completely unknown. Although attractor network

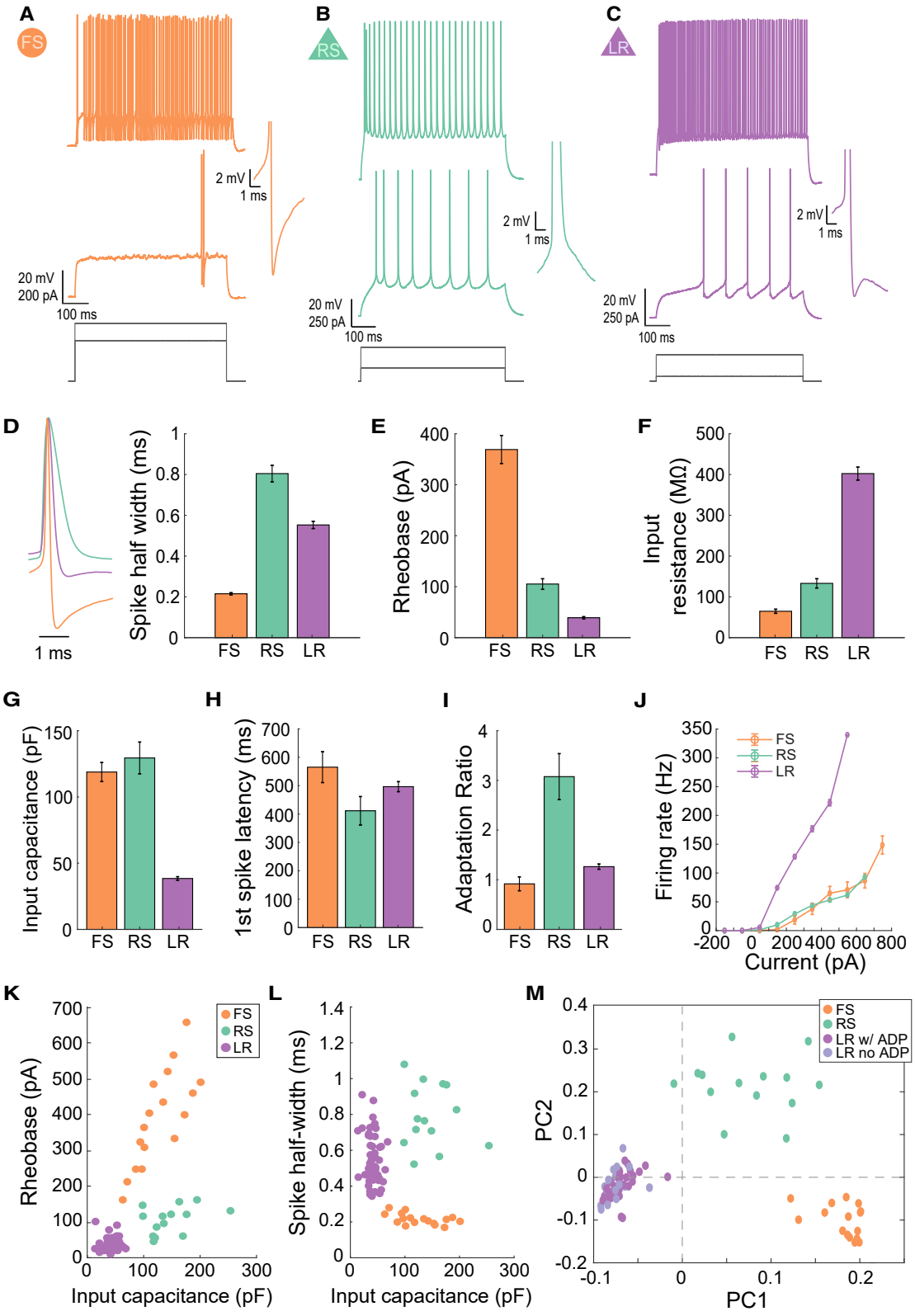

(legend on next page)

models of RSC incorporating generic neurons exist (Bicanski and Burgess, 2016; Page and Jeffery, 2018), it is critical to discover the key intrinsic and local synaptic properties that allow the RSC to perform its specialized functions. Without this information, it is impossible to develop biophysically realistic models of RSC cells or circuits, which would, in turn, help to decipher the exact coding schemes used by the RSC.

Here, we investigate the intrinsic physiology, local synaptic connectivity, and computational abilities of cells within the superficial layers of granular RSC (RSG). The majority of neurons within this region are a distinct subtype of small, highly excitable, non-adapting pyramidal neurons. We show that these cells are excitatory but, surprisingly, rarely excite their neighboring inhibitory or excitatory neurons. Instead, there is prevalent local inhibition from fast-spiking (FS) layers 2/3 (L2/3) neurons onto these highly excitable neurons and between pairs of FS cells, highlighting a network dominated by feedforward, not feedback, inhibition. We then use this information to construct biophysically realistic computational models of RSC cell types and investigate how they process realistic, *in vivo* spike trains of incoming information. We find that these hyperexcitable principal neurons in the RSG are optimally suited to precisely and persistently encode the sustained HD input they receive from the postsubiculum. A smaller population of regular-spiking (RS) excitatory neurons in L2/3 show pronounced adaptation and are unable to maintain such sustained, high-frequency responses. Our results show that there are two complementary coding strategies operating in parallel in the superficial RSC.

RESULTS

Low-rheobase Cells Are Highly Excitable Neurons in the Superficial RSG

We recorded from and parsed the intrinsic physiology of 193 cells in the superficial L2/3 of the mouse RSG. Consistent with other cortical regions, FS interneurons were present in these RSG layers (Figure 1A). FS cells were identified by their unique spiking properties (Connors and Gutnick, 1990; Sempere-Ferràndez et al., 2018), including narrow spike width and rapid, sharp afterhyperpolarizations (AHPs). RS pyramidal neurons were occasionally found, but far less often than in typical neocortex (Figure 1B). A third population of cells was identified. For reasons investigated and explained below, we refer to these distinct neurons as low-rheobase (LR) cells. Detailed analyses of physiological and intrinsic parameters revealed several distinct properties of LR neurons. Statistical differences were calculated using a two-tailed Wilcoxon rank-sum test for all intrinsic comparisons. LR spike widths were between those of FS and RS cells (FS = 0.22 ± 0.05 ms, RS = 0.80 ± 0.04 ms, LR = 0.55 ± 0.02 ms; $p < 0.001$ for each comparison; Figure 1D; Table 1). Additionally, these LR cells had significantly high input resistance (402.35 ± 15.92 MΩ; $p < 0.001$), low input capacitance (38.48 ± 1.33 pF; $p < 0.001$), and LR (40.45 ± 2.07 pA; $p < 0.001$), suggesting they are a class of highly excitable neurons distinct from both FS and RS neurons (Figures 1E–1G; Table 1). LR cells did not differ significantly in latency to first spike from FS ($p = 0.09$) or RS ($p = 0.11$) cells. LR cells also exhibited minimal spike frequency adaptation (ratio of 1.26 ± 0.05), far lower than the substantial spike frequency adaptation shown by RS cells (ratio of 3.07 ± 0.46; $p < 0.001$), highlighting their potential ability to fire trains of action potentials at high frequencies with minimal adaptation (Figure 1I; Table 1). Further supporting this, LR cells showed a dramatically higher slope in their frequency-current relationship (Figure 1J). Additionally, 65% of LR cells exhibited a pronounced afterdepolarization (ADP; Figure 1C) whereas the remaining 35% had no ADP (Table 1). The presence of ADP did not otherwise distinguish the LR cells from those where the ADP was absent. These LR groups did not differ on key intrinsic properties, such as input capacitance, rheobase, or input resistance (as verified using principal-component analysis below).

Figure 1. Low-rheobase Cells Represent a Distinct Highly Excitable Cell Type in the Superficial Retrosplenial Cortex

(A) Intrinsic physiological properties of a fast-spiking (FS) neuron in the superficial layers of the granular retrosplenial cortex. Top trace: ability to fire sustained high-frequency trains of action potentials. Middle trace: a substantial delay to first spike after current onset during a near-threshold current step. Right inset is a zoomed-in view of the first spike in the middle trace. Bottom: injected current amplitudes for the voltage responses shown above.

(B) Similar to (A), but now for a retrosplenial regular-spiking (RS) neuron. Note the spike frequency adaptation characteristic of RS neurons in other cortical regions.

(C) Similar to (A), but now for a retrosplenial low-rheobase (LR) neuron. Note the ability to fire sustained high-frequency trains of action potentials with little spike frequency adaptation.

(D) Left: representative traces from FS, RS, and LR cell action potentials overlaid to show differences in spike width. Right: average spike widths showing that LR spike widths are intermediate to those of neighboring FS and RS ($p < 0.001$ for each comparison).

(E) Average rheobase for FS, RS, and LR cells showing a markedly LR for LR cells compared to that of FS and RS ($p < 0.001$ for each comparison).

(F) Average input resistance (IR) for FS, RS, and LR cells showing a significantly higher IR for LR cells [$p < 0.001$ for each comparison].

(G) Average input capacitance (IC) for FS, RS, and LR cells showing a markedly low IC for LR cells compared to FS and RS ($p < 0.001$ for each comparison).

(H) Bar graph of the average latency to first spike after onset of an at-threshold current injection for FS, RS, and LR cells (LR versus FS, $p = 0.09$; LR versus RS, $p = 0.11$).

(I) Bar graph showing the average spike frequency adaptation ratio for FS, RS, and LR cells showing lack of adaptation in FS and LR cells ($p < 0.001$ for each comparison).

(J) Frequency-current (F-I) curve for FS, RS, and LR neurons highlighting the hyperexcitability of LR neurons.

(K and L) LR cells cluster clearly and separately from FS and RS cells when IC is plotted against either rheobase (K) or spike half-width (L).

(M) Principal-component analysis results in three distinct clusters corresponding to LR, RS, and FS cells. LR cells with and without ADPs cluster together in a single LR cluster.

Error bars represent standard error of the mean. Wilcoxon rank-sum test used for each of the statistical tests reported in this figure.

See also Figure S1 and Table S1.

Table 1. Intrinsic Cell Properties Reveal That LR Cells Have a Distinctly Low Rheobase, High Input Resistance, Low Input Capacitance, and Low Spike Frequency Adaptation, as Well as a Spike Width between Those of FS and RS Cells

	FS		RS		LR	
	Values	n	Values	n	Values	n
Postnatal age at time of recording (days)	25.93 ± 0.43	42	26.65 ± 0.52	26	27.37 ± 0.61	115
Resting potential (mV)	−61.17 ± 0.88	42	−65.12 ± 0.96	26	−66.27 ± 0.64	115
Input resistance (MΩ)	64.68 ± 5.04	28	133.09 ± 11.37	18	402.35 ± 15.92	83
Input capacitance (pF)	118.83 ± 7.19	28	129.46 ± 11.99	18	38.48 ± 1.33	83
Membrane time constant (ms)	7.16 ± 0.58	28	15.35 ± 0.86	18	14.28 ± 0.37	83
Action potential threshold (mV)	−40.73 ± 0.85	35	−40.93 ± 0.87	26	−40.83 ± 0.42	100
Action potential amplitude (mV)	56.86 ± 1.59	35	74.70 ± 2.39	26	64.29 ± 1.03	100
Action potential width (ms)	0.22 ± 0.05	35	0.80 ± 0.04	26	0.55 ± 0.02	100
Afterhyperpolarization amplitude (mV)	17.00 ± 0.54	35	9.74 ± 0.47	26	11.67 ± 0.31 (ADP)	65
					9.88 ± 0.57 (no ADP)	35
Afterhyperpolarization latency (ms)	0.60 ± 0.02	35	25.71 ± 2.74	26	1.39 ± 0.09 (ADP)	65
					9.25 ± 0.48 (no ADP)	35
Spike frequency adaptation ratio	0.92 ± 0.14	35	3.07 ± 0.46	26	1.26 ± 0.05	100
Latency to first spike (ms)	565.14 ± 54.29	31	411.54 ± 50.05	15	496.46 ± 17.71	80
Rheobase (pA)	363.70 ± 28.72	31	105.60 ± 9.62	15	40.45 ± 2.07	80

Values are mean ± SEM for each of the calculated intrinsic properties separated by cell group. Numbers are reported individually for each property for each cell type. LR cells significantly differed from RS cells on the following measures: input resistance, input capacitance, spike width, spike frequency adaptation ratio, and rheobase ($p < 0.001$). LR cells significantly differed from FS cells on the following measures: input resistance, input capacitance, membrane time constant, spike width, AHP amplitude, and rheobase ($p < 0.001$). FS, fast-spiking; RS, regular-spiking; LR, low-rheobase. Related to Figure S1 and Table S1.

To determine whether LR neurons are a truly distinct neuronal subtype, we sought to identify the physiological properties that can clearly distinguish them from other neurons in the superficial RSG. Specifically, using features such as rheobase, input capacitance, and spike width, we were able to isolate LR cells from both FS and RS cells (Figures 1K and 1L). To further verify this clustering among all features simultaneously, we conducted a principal-component analysis (PCA). Upon plotting PC1 versus PC2 (which together account for 97.4% of the variance across all cells), the three cell groups clearly separated into three distinct clusters (Figure 1M). To examine whether the presence or absence of ADPs had any impact on LR classification, we labeled LRs with and without ADPs in separate colors. Both of these groups clustered together as part of the unified LR cluster, with no delineation observed between them. This strongly supports the assertion that LR neurons are one distinct cell type (Figure 1M).

LR Cells Are the Dominant Cell Type in the Superficial RSG

LR neurons were the most commonly encountered cell type in L2/3 of RSG. To quantify the relative percentage of neurons in the superficial RSG, the recorded neurons were assigned to one of four groups based on their intrinsic physiological properties: FS, RS, LR, and unclassified. The unclassified group consisted of 10 neurons whose intrinsic and/or firing properties did not fall under any of the three defined groups (see STAR Methods). We found that LR cells are the dominant cell type in both L2/3, accounting for 61% of the neurons in layer 2 and 59% in layer 3 (Figure 2). However, 0 out of 25 recordings in layers 5 and 6 were of LR cells and instead identified only RS and FS neurons, suggesting that LR neurons are restricted to the superficial layers of RSG (chi-square test, $p < 0.001$; data not shown). In the mouse lines with more than 20 cells recorded, greater than 50% were LR neurons in each line, confirming that LR cells are the dominant cell type in L2/3 of RSC regardless of the mouse line. Surprisingly, the prevalence of RS cells in L2/3 of RSG was extremely low, representing only 26% of all layer 2 neurons and 10% of layer 3 neurons. Indeed, the proportion of LR neurons is significantly greater than that of RS neurons in L2/3 (chi-square test; $p < 0.001$). The FS neuron probabilities are slightly skewed, as experiments detailed later in this manuscript specifically targeted FS interneurons. Thus, the FS neuron probability reported here is likely slightly larger than their true representation in these layers. Nonetheless, it is clear that LR cells are the most prevalent cell type within the superficial layers of the granular RSC, being encountered 4.4 times more often than RS cells.

LR Cells Are Found across the Long Axis of the RSC

The RSC is a large structure, spanning 4.38 mm rostracaudally in mice. In addition to LR cells being the most prevalent cell type, we also found that their expression is consistent across this entire long axis of the RSC (Figure S1B; Table S1). This suggests that the contribution of LR cells to retrosplenial circuit computations is likely to be similar across the long axis of the RSG.

LR Cells Are Found in Both Males and Females at All Ages Examined

LR cells are present in both adolescent and adult mice, suggesting this highly intrinsically excitable cell is not a transient

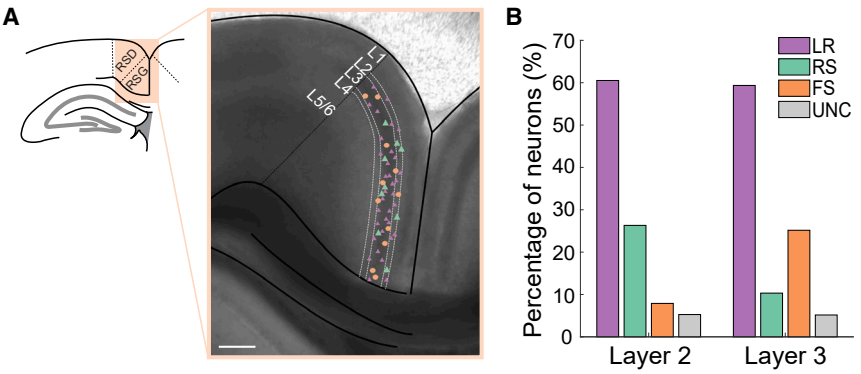

Figure 2. LR Cells Are the Dominant Cell Type in L2/3 of the RSG

(A) Representative anatomy of the RSG and locations of a subset of patched neurons. The left panel shows the location of the retrosplenial cortex superior to the corpus callosum. Right panel shows a differential interference contrast (DIC) image of a retrosplenial mouse brain slice with RSD and RSG separated by a black dotted line. The layers are demarcated by white dotted lines. Small purple triangles, large green triangles, and orange circles denote patch locations of a representative proportion of LR, RS, and FS cells patched in this study, respectively. Scale bar represents 100 μm.

(B) Percentage of each neuronal subtype patched in each layer of RSG. LR cells are the most prevalent cell type in each layer. UNC, unclassified. Layer 2: LR, n = 23; RS, n = 10; FS, n = 3; UNC, n = 2. Layer 3: LR, n = 92; RS, n = 16; FS, n = 39; UNC, n = 8.

developmental phenotype (Figure S1A). LR cells are also found in both male and female mice (Figure S1C). The properties of these neurons do not differ across these different locations, ages, or sex, further supporting their robust existence as a single cell type (Table S1). Thus, these neurons are the dominant cell type in the superficial granular RSC, consistent across age, sex, and long axis of the RSG.

LR Cells Are Excitatory

To investigate whether LR neurons were excitatory or inhibitory, we next conducted whole-cell recordings coupled with optogenetic activation of channelrhodopsin in CaMKIIα+ cells. CaMKIIα-Cre × Ai32 mice (Jackson Laboratories, stock numbers 005359 and 024109, respectively; crossed in house) were used for these experiments. In these mice, cells containing the excitatory marker CaMKIIα express Cre, thus allowing for expression of a cre-dependent channelrhodopsin (ChR2) exclusively in CaMKIIα neurons (Figure 3A). We then used 1-ms light pulses in a 10-Hz train to test ChR2 responses in the patched neurons. Of the LR cells tested, 85% (17/20) directly responded to the optogenetic light pulse, indicating that they were directly expressing ChR2 and, thus, were CaMKIIα positive (Figures 3B and 3C). This suggested, but did not prove, that they may be excitatory neurons.

We then confirmed the excitatory nature of LR cells by using paired recordings of layer 2/3 RSG neurons. Although connections were rare, when LR cells were connected to neighboring FS cells, they led to excitatory post-synaptic potentials (EPSPs) in the paired cell (Figure 4D). This confirms that LR cells in RSG are indeed excitatory neurons.

Dominant Inhibition and Rare Local Excitation in the Superficial Layers of RSG

Using paired whole-cell recordings, we sought to quantify the connectivity between these three major cell types in the superficial layers of RSG: LR and RS (both excitatory; E) and FS (the major inhibitory neurons in these layers; I). To our surprise, LR to FS connectivity was rare (17%), suggesting a relative lack of locally driven excitation of FS cells. On the other hand, FS cells were frequently connected to and inhibited neighboring LR cells (52%) (Figure 4A). When all pairs were considered, the E→I connectivity was only 16%, whereas the I→E connectivity reached 53% (Figure 4B). The difference in probability to observe I→E connections versus E→I connections was significant ($p < 0.001$; two-tailed t test), suggesting the superficial layers of the RSG represents an inhibition-dominated network, with feedforward inhibition far more likely than feedback inhibition. Additionally, we observed no LR→LR connections (0/30), nor any connectivity between LR and RS cells (0/6), indicating a complete lack of E→E connectivity. FS→FS connectivity was robust, being found in each of the 6 directions tested across three pairs (100%; Figure 4A).

The latency to onset of the evoked responses from a holding potential of −55 mV was similar between inhibition and excitation ($p = 0.9273$, Wilcoxon rank-sum test; Figure 4E). However, the peak of the EPSP from LR onto FS cells was reached significantly faster than the peak of IPSPs from FS to LR ($p = 0.0091$, Wilcoxon rank-sum test; n = 3 LR to FS connections; n = 9 FS to LR connections; Figure 4F). IPSPs from FS to LR cells exhibited clear short-term depression. This was seen in paired recordings (Figures 4C and 4G) and also when recording from LR neurons during optogenetic stimulation of FS cells (data not shown). EPSPs from LR to FS cells did not clearly exhibit either depression or facilitation (Figure 4D). The circuit diagram for L2/3 of RSG is summarized in Figure 4H and highlights the prominent role of inhibition in this circuit.

Axons from LR Cells Do Not Ramify Locally but Head to Deeper Layers and toward the Corpus Callosum

The rarity of connections from LR neurons onto their neighboring L2/3 cells suggested that LR axons have more distant targets. To investigate the projections of the LR cells, we used biocytin to fill cells for morphological consideration after characterizing their physiological properties and created 3D reconstructions of the neurons by using Neurolucida. Three representative LR neurons whose cell body, dendrites, and axons were sufficiently filled are shown in Figure 5. All filled LR cells exhibited projections to the deeper layers of RSG (Figures 5F–5I). Axons often clearly entered and traveled within the corpus callosum. Additionally, LR neurons (unlike FS cells) had

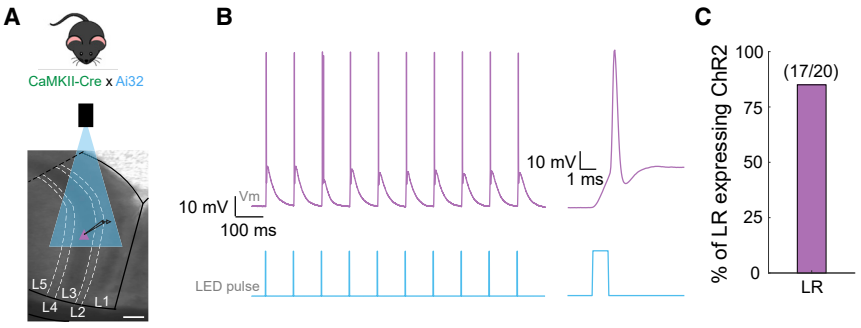

Figure 3. LR Cells Directly Respond to ChR2 in CaMKIIα-Cre × Ai32 Mice, Indicating Expression of CaMKIIα in This Cell Type

(A) Schematic showing the experimental set-up. Top panel: mouse indicating the genetic cross of CaMKIIα-Cre (Jackson Laboratories, stock number 005359) and Ai32 (Jackson Laboratories, stock number 024109; crossed in house). Bottom panel: 10-Hz optical light-emitting diode (LED) pulses were delivered to a whole-cell-patched neuron in L2/3 of RSG while their responses were recorded. Scale bar represents 100 μm.

(B) Representative responses of an LR cell to 10-Hz optical pulses. Left traces show all 10 optical pulses (1 ms each) over the span of 1 s and the LR cell response. Right trace is a zoomed in view of the first optical pulse and resulting spike from the LR cell. The almost instantaneous neuronal response to the light (<0.15-ms latency) is indicative of direct ChR2 expression.

(C) Percentage of LR cells tested that directly expressed ChR2 (85%, 17/20).

very few axonal ramifications within L2/3, matching their extremely low likelihood to synapse onto local neurons (Figures 5F, 5G, and 5I). Upon further examination of our four paired recordings in which LR cells directly excited the paired FS cell, we noted that all of these LR cells were located more superficially than their paired FS cell. Conversely, of the four pairs in which the FS cell was located more superficial to the LR cell, none exhibited connections from the LR to the FS cell. This supports the finding that LR axons immediately travel to deeper areas and do not ramify locally or superficial to their cell bodies. It also suggests that FS cells in L2, even more so than L3 FS cells, are likely to be completely devoid of local excitation from LR cells.

Because LR neurons are pyramidal, we also sought to compare their morphology to neighboring pyramidal RS neurons (Figure 5A), which exhibit extremely different electrophysiological properties. Sholl analysis revealed distinct dendritic morphologies of the two pyramidal cell types, with RS neurons having significantly more intersections up to 150 μm from the soma (Figure 5B). To further investigate these differences, we measured key morphological characteristics and found that RS cells were indeed significantly larger than LR neurons, having larger cell bodies, longer dendrites, and a greater number of dendritic branches (Figures 5C, 5D,and 5E). These morphological differences between RS and LR cells reinforce their physiological differences and further support the characterization of LR cells as a distinct cell type.

LR Neurons Support High-Fidelity, Sustained Responses to Persistent HD Inputs

We next created biophysically realistic models of both RS and LR cells (see STAR Methods). The morphology of both the RS and LR neuron models were based on anatomical reconstructions of their experimental counterparts (Figures 6A and 6E). Experimental physiological properties were accurately reproduced in each model (Figures 6B and 6F), with the LR neuron model having a higher input resistance, minimal spike frequency adaptation, and narrower spike width than the RS neuron model (Figures 6C and 6G). Frequency-current responses and latency-current response of the neuron models also closely corresponded to the experimental data for each neuronal subtype (Figures 6D and 6H).

We then used these biophysically realistic models to understand the information processing capabilities of LR versus RS neurons. The subdivisions of the subicular complex provide some of the most prominent sources of input to the superficial layers of the RSC (Wyss and Van Groen, 1992; Van Groen and Wyss, 2003; Yamawaki et al., 2019a). Many cells in the postsubiculum fire selectively when an animal is facing a particular direction and are, hence, called HD cells (Taube et al., 1990). These postsubicular HD cells are bursty, firing a series of rapid spikes at rates of 100–250 Hz (Funahashi and Stewart, 1997; Peyrache et al., 2015). The same postsubicular HD cells also fire long-duration, persistent trains of action potentials (Taube and Bassett, 2003; Yoshida and Hasselmo, 2009; Peyrache et al., 2015). This persistent firing is thought to be critical for maintaining a sense of orientation when the animal is not moving but instead continuously facing a particular direction (Taube and Bassett, 2003; Yoshida and Hasselmo, 2009; Peyrache et al., 2015).

We sequentially examined how these important properties of postsubicular inputs are processed by RS versus LR neurons. First, 200-Hz bursts consisting of 5 spikes were input into both RS and LR cell models (Figures 7A and 7B). The RS cell response to each of the constituent spikes within the burst was characterized by a low probability of firing and imprecisely timed action potentials (high jitter). LR cells, on the other hand, responded with high reliability and more precisely timed action potentials with little jitter across trials (Figures 7C–7F), as would be expected based on their much higher input resistance. LR cell spikes were significantly more reliable and more precise (less jitter) than RS cell spikes in response to the burst input ($p < 0.001$; two-tailed t test), showing that LR neurons are capable of higher fidelity burst encoding with superior spike timing coding capabilities than their neighboring RS neurons. Qualitatively similar results were obtained when the g_{max} of synaptic inputs was halved in strength (data not shown).

We next examined the ability of LR and RS neurons to respond to persistent inputs of varying durations. First, we utilized a continuous input spike train of 200 Hz over progressively longer durations. LR cells were able to respond with high probability and high precision for all durations examined (Figure 7G). RS cells, on the other hand, had average

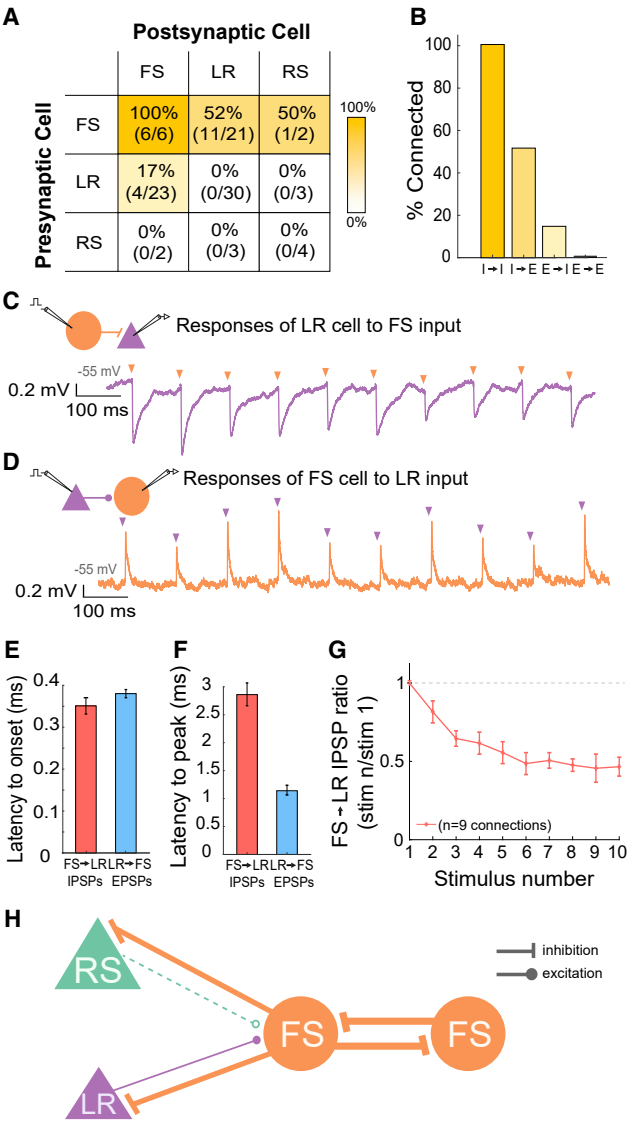

Figure 4. Dominant Local Inhibition in the Superficial Layers of the Retrosplenial Cortex

(A) Table indicating the percentage of connectivity between all types of pairs tested. The heatmap indicates the probability of connections between the neuron types indicated in each cell of the table.

(B) Total connectivity probability between all I→I directional pairs (100%), I→E directional pairs (52%), E→I directional pairs (16%), and E→E directional pairs (0%). Bootstrap resampling followed by a t test revealed a significantly higher likelihood of observing I→E connections versus E→I connections ($p < 0.001$).

(C) Representative trace of the connection between a presynaptic L3 FS cell and a postsynaptic L3 LR cell (held at −55 mV). The neurons were 27 μm apart, with the LR cell located superficial to the FS cell. Schematic shows the patched pair in which the FS cell is being stimulated to spike at 10 Hz, with postsynaptic potentials recorded in the LR cell. The purple trace is the response of the LR cell to a 10-Hz sequence of FS cell spikes (indicated by orange arrows).

(D) Similar to (C), but now for a presynaptic LR to postsynaptic FS excitatory connection.

(E) Average latency to onset of the IPSPs recorded from the FS→LR pairs (red) and the EPSPs recorded from the LR→FS pairs (blue) ($p = 0.9273$, Wilcoxon rank-sum test). Error bars represent standard error.

(F) Average latency to peak of the IPSPs recorded from the FS→LR pairs (red) and the EPSPs recorded from the LR→FS pairs (blue) ($p = 0.009$, Wilcoxon rank-sum test). Error bars represent standard error.

(G) Group synaptic dynamics for FS→LR connections ($n = 9$). Inhibition onto LR cells exhibited strong short-term depression.

(H) Schematic of the microcircuitry of FS, RS, and LR cells in the superficial layers of RSG.

response probabilities under 0.45, even when we removed the adaptation current from the RS cell model. Signal-to-noise ratio (SNR) analyses (see STAR Methods) showed that the LR cell response was characterized by high SNR to prolonged 200-Hz inputs (Figure 7H). RS cells, with and without adaptation, showed several fold lower SNR for both short and long durations (Figure 7H). The ratio of SNR for LR response (SNR_{LR}) to SNR for RS response (SNR_{RS}) progressively increased at higher input durations (Figure 7H, inset), indicating the progressive failure of RS cells to reliably encode longer duration inputs with enough spikes. When we removed the adaptation current from the RS cell model, the ratio SNR_{LR} to SNR for the RS model without adaptation ($SNR_{RS\text{-}No\text{-}Adap}$) remained very high but did not progressively increase as a function of increasing input durations (Figure 7H, inset), indicating that the spike frequency adaptation of RS neurons prevents reliable transmission of long duration, persistent inputs to its postsynaptic targets. These results suggest that a combination of passive and active properties enables LR neurons to have higher fidelity, sustained SNR at high input durations. The spike frequency adaptation of RS neurons amplifies the SNR disadvantage of RS neurons at longer durations. The SNR results held true even when we increased the stimulation frequency of background synaptic inputs to 10 or 20 Hz (Figure S2), suggesting our results were robust to variations in these model parameters.

Finally, we validated our models' predictions by utilizing realistic input spike trains recorded from HD cells in the postsubiculum (Figure 7I; Peyrache and Buzsaki, 2015). As expected, this dataset included epochs of persistent, long-duration firing when the animal faced a given cell's preferred HD. A typical postsubicular neuron had an intra-burst frequency of ~100 Hz, based upon the inter-spike-interval (ISI) histogram (Figure S3A). The LR neuron model exhibited a higher probability of firing and greater spike timing precision than the RS neuron model when stimulated with spike trains corresponding to this peak firing rate in this dataset, further affirming the superior encoding capabilities of the LR neuron model (Figures S3B–S3D). We found that LR neurons encoded this postsubiculum HD input with higher SNR at all input durations. The ratio of SNR_{LR} to SNR_{RS} again increased dramatically at higher input durations (when the animal faced the same direction for long periods of time; Figure 7J), indicating the inability of RS neurons to faithfully encode persistent, long duration inputs coming from the postsubicular HD cells.

LR and RS neurons are characterized by different dendritic morphologies and branching patterns in terms of number of branches and total branch length (Figures 5B–5D). As a result, synaptic inputs can undergo differential filtering, as inputs

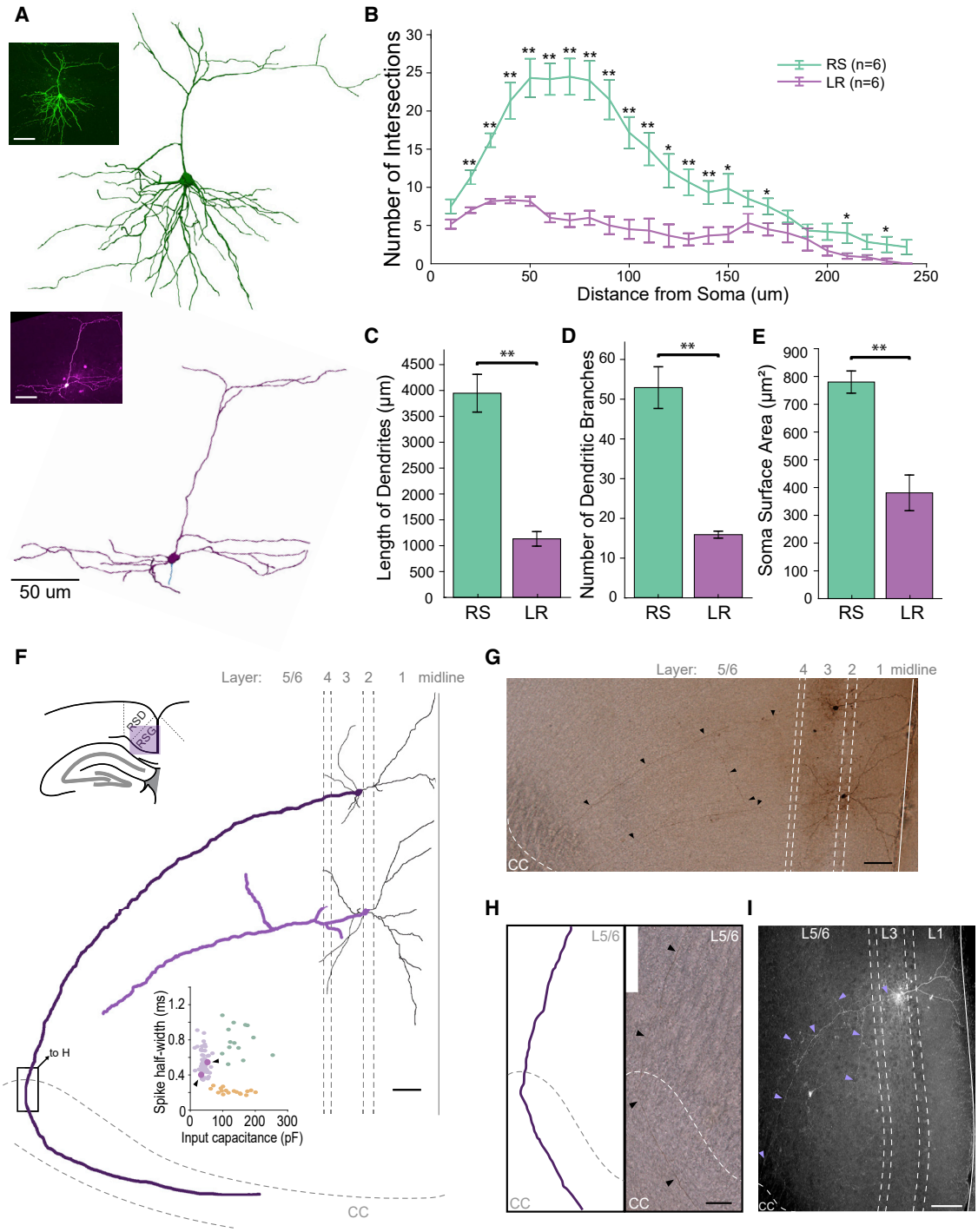

Figure 5. LR Axons Do Not Ramify Locally and Instead Project to Deeper Layers and the Corpus Callosum

(A) Fluorescent fills and subsequent Neurolucida reconstructions of an example RS (green) and LR (purple) neuron. Scale bar represents 50 µm.

(B) Sholl analysis of the total dendrites of RS (green) and LR (purple) neurons in L2/3 of RSG (*p < 0.05; **p < 0.01; Wilcoxon rank-sum test).

(C) Total length of dendrites for RS (green) and LR (purple) neurons (**p < 0.01, Wilcoxon rank-sum test).

(D) Same as (C) for number of dendritic branches (**p < 0.01, Wilcoxon rank-sum test).

(E) Same as (C) for soma surface area (**p < 0.01, Wilcoxon rank-sum test).

(F) Schematic of the axonal ramifications of two L2/3 LR neurons. Top left shows the location of the RSC within the −1.8-mm AP slice in a P25 mouse. Layers and corpus callosum are demarcated by gray dashed lines. Scale bar represents 50 µm. Dendrites are in black, and cell bodies/axons are in purple. Axons project clearly to deeper layers, often entering the corpus callosum. Minimal axonal ramifications are observed in L2/3. Inset is identical to that in Figure 1L with the two LR cells referenced here in larger purple dots, indicated by the arrows.

(legend continued on next page)

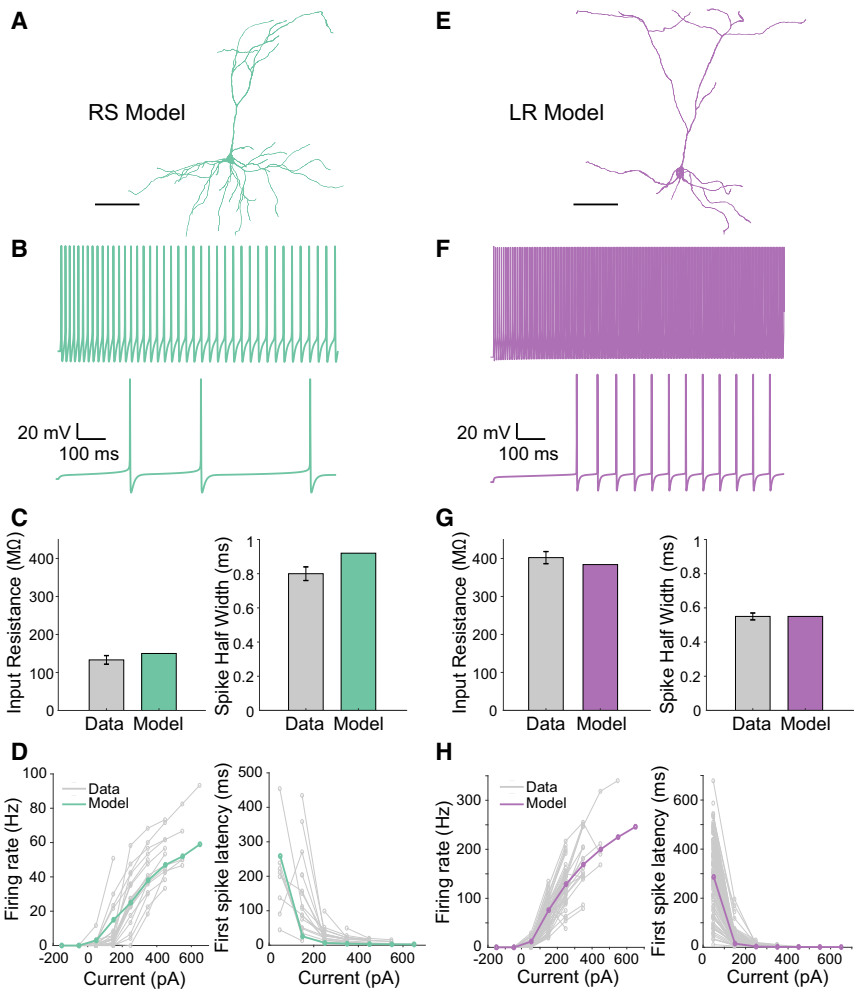

Figure 6. Computational Models of LR and RS Neurons Accurately Replicate the Physiological and Morphological Properties of the Respective Neuronal Subtypes

(A) Morphology of the corresponding RS neuron model. Scale bar represents 50 μm.

(B) Response of the RS neuron model to a low (50 pA) and high (400 pA) current injection.

(C) Left: IR of the RS neuron model (green; 148 MΩ) compared to the average IR of the physiologically recorded RS cells (gray; 133.09 MΩ). Right: spike width of the RS neuron model (green; 0.92 ms) compared to the average spike width of the physiologically recorded RS cells (gray; 0.80 ms).

(D) Left: similar F-I relationships for the model (green) and physiologically recorded (gray) RS cells. Right: latency to first spike-current (L-I) relationship for the model (green) and physiologically recorded (gray) RS cells.

(E) Morphology of the LR neuron model. Scale bar represents 50 μm.

(F) Modeled LR cell response to a low (50 pA) and high (400 pA) current injection.

(G) Left: IR of the LR neuron model (purple; 384 MΩ) compared to the average IR of the physiologically recorded LR cells (gray; 402.35 MΩ). Right: spike width of the LR neuron model (purple; 0.55 ms) compared to the average spike width of the physiologically recorded LR cells (gray; 0.55 ms).

(H) Left: similar F-I relationship for the model (purple) and physiologically recorded (gray) LR cells. Right: L-I relationship for the model (purple) and physiologically recorded (gray) LR cells.

See also Table S2.

arriving at apical portions of the dendritic tree are filtered more at the soma than proximal inputs (Häusser, 2001). To ensure that the differences in SNR between the LR and RS neuron models are not due to their differential dendritic filtering properties, we normalized the synaptic inputs such that their location dependence was eliminated. Even after normalizing the synaptic inputs, the LR neuron model had superior SNR compared to the RS neuron model, and the difference became larger when the input duration was increased (Figure S4A). The same result was observed when the two models were stimulated with realistic *in vivo* input spike trains (Figure S4B). These results indicate that SNR differences between the two neuronal subtypes are primarily due to differences in their intrinsic properties and not due to morphological differences. Thus, LR neurons are better suited to encode persistent inputs, such as those involved in long-duration HD signaling, than RS neurons.

DISCUSSION

The unique cytoarchitecture of the RSC has long been appreciated by neuroanatomists (Rose, 1927; Van Groen and Wyss, 2003; Wyss et al., 1990; Wyss and Van Groen, 1992; Ichinohe and Rockland, 2002). The granular division of the RSC, in particular, has two geometric features that appear to set it apart from many other cortical regions: (1) small pyramidal neurons that cluster most densely in L2/3 (Wyss et al., 1990; Kurotani et al., 2013) and (2) the bundling of apical dendrites emanating from these small L2/3 pyramidal neurons (Wyss et al., 1990; Ichinohe and Rockland, 2002). Thus, a thorough understanding of granular RSC function would greatly benefit from an in-depth understanding of these distinct L2/3 neurons.

Here, we have characterized the detailed intrinsic properties, connectivity, and computational capabilities of these small

(G) Biocytin fill used to create the schematic in (F). Arrows are placed periodically along the axon for visualization. Scale bar represents 50 μm.

(H) Zoomed in view of the box indicated in (F). Left shows a schematic of the axon projecting through L5/6 before entering and traveling within the corpus callosum. Right shows biocytin fill image. Arrows are placed periodically along the axon for visualization. Scale bar represents 50 μm.

(I) Fluorescent fill of an LR cell with axonal projection to the corpus callosum. Arrows are used to visualize the projecting axon and minor ramifications in deeper layers. Scale bar represents 100 μm.

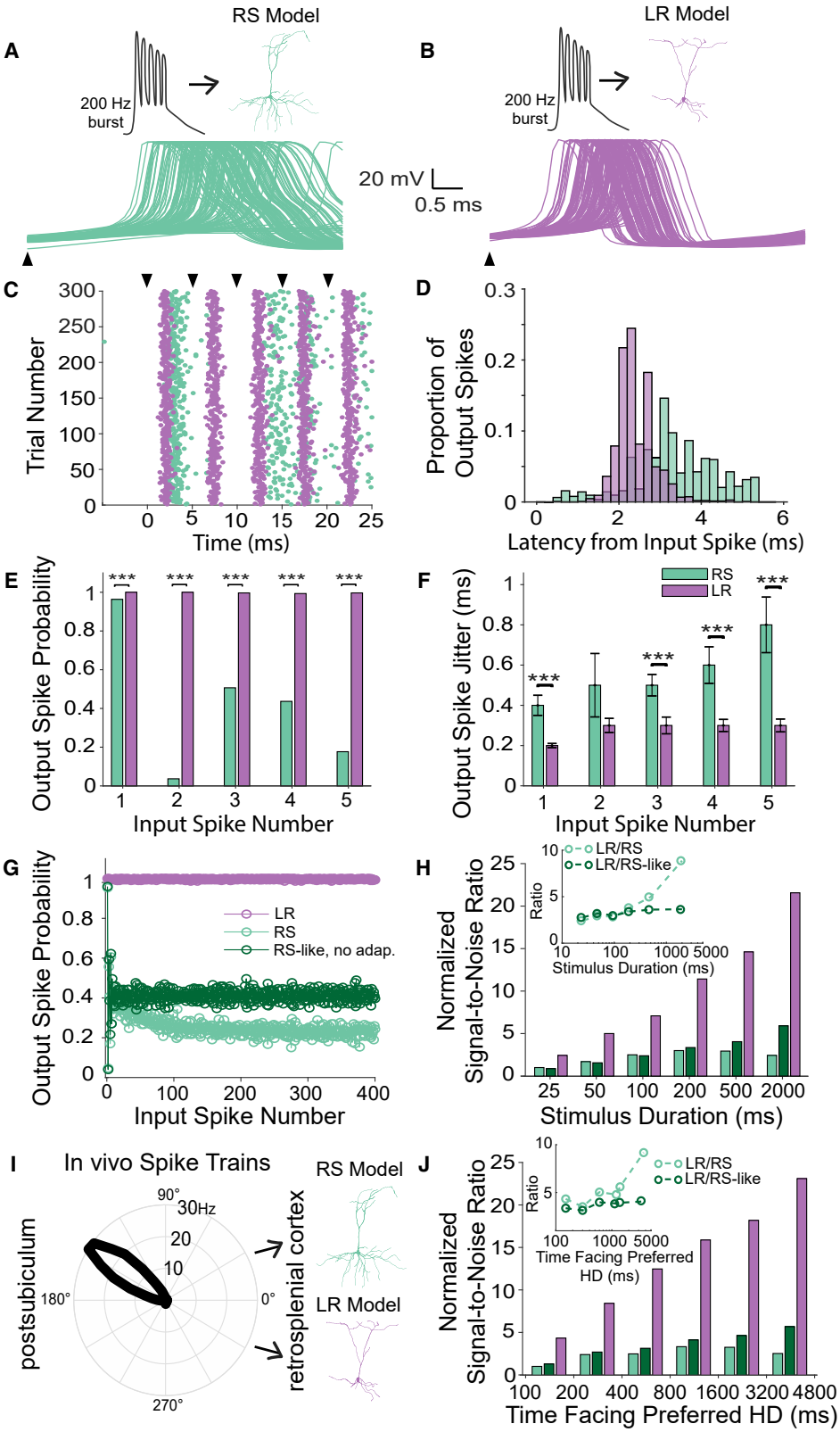

(legend on next page)

pyramidal cells, as well as their neighboring, larger, more familiar RS cells, revealing a number of key differences. We call these small pyramidal cells LR neurons based upon the ease with which they can be excited and made to fire (due, in large part, to their high input resistance). In addition to their high excitability, these cells also have spike widths that are much narrower than RS cells and show minimal spike frequency adaptation, again in sharp contrast to RS neurons (Figure 1; Table 1). We also found that all three cell types examined had a tendency to spike late during a near threshold current injection, consistent with high levels of Kv1.1 or Kv1.2 ion channel expression in the RSC (Kurotani et al., 2013). There was no significant difference in the first spike latency of LR versus RS cells (Figure 1; Table 1). Thus, the key, defining computational features of LR cells are their hyperexcitability and lack of spike frequency adaptation.

How do the distinct passive and active properties of LR versus RS neurons impact their input-output transformations and information-coding capabilities? We used biophysically realistic models to investigate this question. On the short timescale, the higher excitability and shorter spike widths of LR cells enable them to spike with a higher probability and lower jitter in response to incoming bursts of spikes (Figures 7A–7F), such as those generated by afferent postsubicular cells during active behaviors (Simonnet and Brecht, 2019). On the long timescale, the almost complete lack of spike frequency adaptation helps LR cells maintain sustained (and still precise) responses to incoming persistent inputs (Figures 7G–7J). This encoding of persistent information appears critical to the function of the RSC. Recent imaging evidence suggests that RSC neurons (generically defined, irrespective of subtype) have a unique ability to encode long-duration, history-dependent value signals (Hattori et al., 2019). Of even more direct relevance is the persistent nature of the navigational information being processed by the superficial RSC. The subicular complex, including the postsubiculum, represents one of the key functional inputs to RSC L2/3 cells (Wyss and Van Groen, 1992; Yamawaki et al., 2019b, 2019a). Postsubicular neurons display a strong preference for particular orientations and are, thus, called HD cells (Taube et al., 1990). When an animal faces a particular direction for long durations, postsubiculum HD cells keep spiking persistently, likely contributing to the maintenance of the sense of orientation in the absence of ongoing vestibular changes (Taube et al., 1990; Yoshida and Hasselmo, 2009). The distinct properties of LR cells suggest they are ideally suited to respond to this persistent postsubicular input (Figures 7I and 7J), enabling the retrosplenial circuit to utilize this valuable HD input to help generate a sense of orientation regardless of how long an animal has been facing the same direction. In fact, our results suggest that the longer an animal faces a postsubicular cell's preferred direction, the better the SNR with which LR neurons can encode this information (due to the accumulation of high-rate signal spikes over time), potentially helping to increase the behavioral certainty of the current orientation and helping to recall orientation-relevant memories. Indeed, a sense of spatial disorientation is one of the key deficits after RSC damage in humans (Bottini et al., 1990; Takahashi et al., 1997; Ino et al., 2007; Osawa et al., 2007).

Several lines of future work are needed to better understand LR versus RS neuronal processing in support of RSC function. It is not yet known whether postsubicular cells differentially contact LR versus RS cells. Nor do we yet know the short-term dynamics of postsubicular inputs to LR versus RS cells. Perhaps the single most important gap in the field's knowledge regarding L2/3 RSC neurons is the lack of any information on their *in vivo* spike patterns and how their firing encodes navigation and memory-related information. No *in vivo* awake, behavioral recordings to date have specifically attempted to precisely target L2/3 of the granular RSC, likely due to its relatively inaccessible position at the midline. Our precise characterization of differences in spike width and adaptation between LR and RS neurons will help the field to identify these distinct neurons by using precisely planned extracellular recordings.

The presence of two distinct, neighboring principal neurons is seen in several structures that are important for spatial navigation and memory. Recent work has shown that granule and mossy cells in the dentate gyrus differentially encode spatial information (Scharfman, 1992, 2019; GoodSmith et al., 2017;

Figure 7. Unique Properties of LR Neurons Enable High-Fidelity, Sustained Encoding of Persistent Head-Direction Input

(A) Top: schematic of a 200-Hz, 5-spike burst input to the RS neuron model. Bottom: membrane potential traces of the RS neuron in response to first spike of the burst input across 300 trials.

(B) Top: similar to (A), but now for the LR neuron model.

(C) Raster plot of the firing of RS and LR neuron models in response to the burst input. The RS model response is characterized by low reliability and lack of spike timing precision, whereas the LR model fires with high reliability and high spike timing precision.

(D) Distribution of spike latencies of the RS (green) and LR (purple) models for all five spikes within the burst input, highlighting the precise timing of LR responses.

(E) Output spike probability of the RS (green) and LR (purple) models to each individual spike within the burst. The LR model has a significantly higher probability of responding to each spike within the burst compared to the RS model (***$p < 0.001$, Pearson chi-square test).

(F) Spike timing precision computed as the jitter in the output spikes for the RS (green) and LR (purple) models to each individual spike within the burst. The LR model is characterized by high spike timing precision compared to the RS model (***$p < 0.001$, two-tailed t test).

(G) Output spike probability of the LR model and two RS models (a standard model and a second RS-like model without spike frequency adaptation) as a function of input spike number for a 2-s continuous stimulation. Note the diminished spike probability on both RS models, compared to the highly reliable LR responses.

(H) Signal-to-noise ratio (SNR) of RS (with and without spike frequency adaptation) and LR neuron models as a function of the duration of the input stimulus. Inset represents the ratio of SNR of the LR neuron model to the SNR of the two RS neuron models.

(I) Schematic of *in vivo* head-direction input from the postsubiculum to the modeled RS and LR neurons. Polar plot shows the *in vivo* head-direction tuning of the input postsubiculum head-direction cell.

(J) Same as (H), but now in response to realistic *in vivo* spike trains of the postsubiculum head-direction cell shown in (I). LR, but not RS, neurons encode persistent head-direction inputs with high SNR.

See also Figures S2, S3, and S4.

Senzai and Buzsáki, 2017), resolving several previously confusing data points regarding the nature of the sparse code used by granule cells (Leutgeb et al., 2007). Similarly, neighboring deep versus superficial CA1 pyramidal cells have been shown to have differential spatial and temporal firing properties, as well as distinct local and distant connectivity (Mizuseki et al., 2011; Lee et al., 2014; Danielson et al., 2016; Soltesz and Losonczy, 2018). In the subiculum, the cells show two distinct patterns of bursting as well as differences in VGlut1 versus VGlut2 expression (Simonnet and Brecht, 2019; Yamawaki et al., 2019a). Thus, the notion of parallel coding schemes implemented by distinct populations of principal neurons is of clear importance in regions involved in memory and navigation. In the superficial RSC, our results show that such parallel neural codes are likely to be implemented by the distinct properties of LR and RS neurons. The intrinsic properties of LR and RS cells are likely to make them better suited to encode persistent versus rapidly changing inputs, respectively. We, thus, hypothesize that RS cells in L2/3 of RSG are likely to better encode information during active head rotations and movement, whereas LR cells may be better suited to integrating long-duration persistent HD and position information when the animal is not moving (as shown in Figure 7). Indeed, our results predict that the longer an animal faces a particular direction, the higher the SNR with which LR neurons can encode this information. Thus, LR neurons may contribute heavily to retaining the current directional bearing when initiating the next movement. In addition to the postsubiculum, the RSC receives inputs from several other regions, including directional information from the anterior thalamus (Taube, 1995; Peyrache et al., 2015) and positional and route-based information from the dorsal subiculum and posterior parietal cortex (Sharp and Green, 1994; Sharp, 1999; Nitz, 2006; Kim et al., 2012; Stewart et al., 2013; Wilber et al., 2014; Cullen and Taube, 2017; Olson et al., 2017; Simonnet and Brecht, 2019). Regardless of the precise content of the information being conveyed by these sources, our results indicate the LR neurons are more suited to integrating this information over longer timescales, potentially helping the RSC encode a sense of long-duration spatial orientation and bearing—a sense that manifests itself as confidently knowing where one is and which way one is looking.

Our paired recordings provide direct proof that LR neurons are indeed excitatory (Figures 3 and 4). Although LR cells are the most prevalent cell type in L2/3 (Figure 2), they make few local connections (Figure 4), instead sending their axons into the deeper layers and corpus callosum (Figure 5). LR cells receive prominent inhibitory inputs from the neighboring L2/3 FS cells (Figure 4), with the probability of FS-to-LR connectivity reaching 52%, which is somewhat higher than that reported in many other regions of the neocortex (Beierlein et al., 2003; Yoshimura and Callaway, 2005; Packer and Yuste, 2011; Jiang et al., 2015). This finding, coupled with the complete lack of local excitatory connections onto LR cells (Figure 4) and the dense FS-FS connectivity (Figure 4), indicates that the superficial layers of the RSG are a network dominated by local inhibition. The inhibition from FS to LR neurons showed similar short-term depression to that seen from FS to RS cells in many other cortical structures (Figure 4G; Beierlein et al., 2003). Our study had a low number of RS-FS pairs sampled, and their connectivity will be precisely quantified in future work. Although we did not explicitly model feedforward inhibition in our simulations, this depression is likely to further aid in the long-duration firing of LR neurons in response to persistent postsubicular inputs by curtailing the strength of feedforward inhibition over time. Of importance to network computations, the strong FS-FS and FS-LR connectivity is also likely to allow the RSC circuit to implement high-frequency oscillations that are generated by the interneuron-gamma (ING) mechanism, instead of, or in addition to, oscillations generated by the pyramidal-ING (PING) mechanism (Koike et al., 2017; Alexander et al., 2018). Future large-scale circuit models of the superficial RSC incorporating LR, RS, and FS cells based on the intrinsic properties and connectivity principles described here will help us to understand the network computations performed by this unique retrosplenial circuit (Figure 4H).

STAR★METHODS

Detailed methods are provided in the online version of this paper and include the following:

- KEY RESOURCES TABLE
- LEAD CONTACT AND MATERIALS AVAILABILITY
- EXPERIMENTAL MODEL AND SUBJECT DETAILS
- METHOD DETAILS
  - Physiological Experimental Methods
  - Computational Modeling Methods
  - LR neuron model
  - Fast sodium current
  - Delayed rectifier potassium current
  - K_v1 current
  - Adaptation current
  - RS neuron model
  - Fast sodium current
  - Delayed rectifier potassium current
  - K_v1 current
  - Adaptation current
- QUANTIFICATION AND STATISTICAL ANALYSIS
  - Experimental Analysis and Statistics
  - Computational Analysis and Statistics
- DATA AND CODE AVAILABILITY

SUPPLEMENTAL INFORMATION

Supplemental Information can be found online at https://doi.org/10.1016/j.celrep.2019.12.093.

ACKNOWLEDGMENTS

We would like to thank Barry Connors, Scott Cruikshank, Wayne Aldridge, and Vaughn Hetrick for their comments on the manuscript; Michael Roberts for his assistance with Neurolucida; and Vaughn Hetrick for his technical assistance. This work was supported by startup funds from the University of Michigan to O.J.A. and by NSF graduate research fellowships to both E.K.W.B. and T.T.J.

AUTHOR CONTRIBUTIONS

Conceptualization, O.J.A., E.K.W.B., and S.K.S.; Methodology, O.J.A., E.K.W.B., and S.K.S; Investigation, E.K.W.B., S.K.S., and I.J.-C.; Software, S.K.S. and O.J.A.; Formal Analysis, E.K.W.B., S.K.S., and T.T.J.; Visualization, E.K.W.B., S.K.S., I.J.-C., T.T.J., and O.J.A.; Writing – Original Draft, O.J.A. and E.K.W.B.; Writing – Review and Editing, O.J.A., E.K.W.B., S.K.S., I.J.-C., and T.T.J.; Funding Acquisition, O.J.A.; Supervision, O.J.A.

DECLARATION OF INTERESTS

The authors declare no competing interests.

Received: June 28, 2019
Revised: October 25, 2019
Accepted: December 27, 2019
Published: February 4, 2020

REFERENCES

A. Agresti, ed. (2007). An Introduction to Categorical Data Analysis, Second Edition (Wiley-Interscience).

Alexander, A.S., and Nitz, D.A. (2015). Retrosplenial cortex maps the conjunction of internal and external spaces. Nat. Neurosci. *18*, 1143–1151.

Alexander, A.S., Rangel, L.M., Tingley, D., and Nitz, D.A. (2018). Neurophysiological signatures of temporal coordination between retrosplenial cortex and the hippocampal formation. Behav. Neurosci. *132*, 453–468.

Beierlein, M., Gibson, J.R., and Connors, B.W. (2003). Two dynamically distinct inhibitory networks in layer 4 of the neocortex. J. Neurophysiol. *90*, 2987–3000.

Bicanski, A., and Burgess, N. (2016). Environmental Anchoring of Head Direction in a Computational Model of Retrosplenial Cortex. J. Neurosci. *36*, 11601–11618.

Bottini, G., Cappa, S., Geminiani, G., and Sterzi, R. (1990). Topographic disorientation—a case report. Neuropsychologia *28*, 309–312.

Buckley, M.J., and Mitchell, A.S. (2016). Retrosplenial Cortical Contributions to Anterograde and Retrograde Memory in the Monkey. Cereb. Cortex *26*, 2905–2918.

Cho, J., and Sharp, P.E. (2001). Head direction, place, and movement correlates for cells in the rat retrosplenial cortex. Behav. Neurosci. *115*, 3–25.

Chrastil, E.R. (2018). Heterogeneity in human retrosplenial cortex: a review of function and connectivity. Behav. Neurosci. *132*, 317–338.

Connors, B.W., and Gutnick, M.J. (1990). Intrinsic firing patterns of diverse neocortical neurons. Trends Neurosci. *13*, 99–104.

Cruikshank, S.J., Ahmed, O.J., Stevens, T.R., Patrick, S.L., Gonzalez, A.N., Elmaleh, M., and Connors, B.W. (2012). Thalamic control of layer 1 circuits in prefrontal cortex. J. Neurosci. *32*, 17813–17823.

Cullen, K.E., and Taube, J.S. (2017). Our sense of direction: progress, controversies and challenges. Nat. Neurosci. *20*, 1465–1473.

Czajkowski, R., Jayaprakash, B., Wiltgen, B., Rogerson, T., Guzman-Karlsson, M.C., Barth, A.L., Trachtenberg, J.T., and Silva, A.J. (2014). Encoding and storage of spatial information in the retrosplenial cortex. Proc. Natl. Acad. Sci. USA *111*, 8661–8666.

Danielson, N.B., Zaremba, J.D., Kaifosh, P., Bowler, J., Ladow, M., and Losonczy, A. (2016). Sublayer-Specific Coding Dynamics during Spatial Navigation and Learning in Hippocampal Area CA1. Neuron *91*, 652–665.

de Sousa, A.F., Cowansage, K.K., Zutshi, I., Cardozo, L.M., Yoo, E.J., Leutgeb, S., and Mayford, M. (2019). Optogenetic reactivation of memory ensembles in the retrosplenial cortex induces systems consolidation. Proc. Natl. Acad. Sci. USA *116*, 8576–8581.

Dégenètais, E., Thierry, A.-M., Glowinski, J., and Gioanni, Y. (2002). Electrophysiological properties of pyramidal neurons in the rat prefrontal cortex: an in vivo intracellular recording study. Cereb. Cortex *12*, 1–16.

Duguid, I., Branco, T., London, M., Chadderton, P., and Häusser, M. (2012). Tonic inhibition enhances fidelity of sensory information transmission in the cerebellar cortex. J. Neurosci. *32*, 11132–11143.

Epstein, R.A. (2008). Parahippocampal and retrosplenial contributions to human spatial navigation. Trends Cogn. Sci. *12*, 388–396.

Erisir, A., Lau, D., Rudy, B., and Leonard, C.S. (1999). Function of specific K(+) channels in sustained high-frequency firing of fast-spiking neocortical interneurons. J. Neurophysiol. *82*, 2476–2489.

Fuhrmann, G., Markram, H., and Tsodyks, M. (2002). Spike frequency adaptation and neocortical rhythms. J. Neurophysiol. *88*, 761–770.

Funahashi, M., and Stewart, M. (1997). Presubicular and parasubicular cortical neurons of the rat: functional separation of deep and superficial neurons in vitro. J. Physiol. *501*, 387–403.

Goldberg, E.M., Clark, B.D., Zagha, E., Nahmani, M., Erisir, A., and Rudy, B. (2008). K+ channels at the axon initial segment dampen near-threshold excitability of neocortical fast-spiking GABAergic interneurons. Neuron *58*, 387–400.

Golomb, D., Donner, K., Shacham, L., Shlosberg, D., Amitai, Y., and Hansel, D. (2007). Mechanisms of firing patterns in fast-spiking cortical interneurons. PLoS Comput. Biol. *3*, e156.

GoodSmith, D., Chen, X., Wang, C., Kim, S.H., Song, H., Burgalossi, A., Christian, K.M., and Knierim, J.J. (2017). Spatial Representations of Granule Cells and Mossy Cells of the Dentate Gyrus. Neuron *93*, 677–690.e5.

Guan, D., Tkatch, T., Surmeier, D.J., Armstrong, W.E., and Foehring, R.C. (2007). Kv2 subunits underlie slowly inactivating potassium current in rat neocortical pyramidal neurons. J. Physiol. *581*, 941–960.

Hattori, R., Danskin, B., Babic, Z., Mlynaryk, N., and Komiyama, T. (2019). Area-Specificity and Plasticity of History-Dependent Value Coding During Learning. Cell *177*, 1858–1872.e15.

Häusser, M. (2001). Synaptic function: dendritic democracy. Curr. Biol. *11*, R10–R12.

Heilman, K.M., and Sypert, G.W. (1977). Korsakoff's syndrome resulting from bilateral fornix lesions. Neurology *27*, 490–493.

Henseler, J., Ringle, C.M., and Sinkovics, R.R. (2009). The use of partial least squares path modeling in international marketing. In New Challenges to International Marketing (Advances in International Marketing, Vol. 20), R. Sinkovics and P. Ghauri, eds. (Emerald Group Publishing), pp. 277–319.

Hille, B. (2001). Ion Channels of Excitable Membranes, Third Edition (Sinauer Associates).

Hines, M.L., and Carnevale, N.T. (2001). NEURON: a tool for neuroscientists. Neuroscientist *7*, 123–135.

Hodgkin, A.L., and Huxley, A.F. (1952). A quantitative description of membrane current and its application to conduction and excitation in nerve. J. Physiol. *117*, 500–544.

Ichinohe, N., and Rockland, K.S. (2002). Parvalbumin positive dendrites colocalize with apical dendritic bundles in rat retrosplenial cortex. Neuroreport *13*, 757–761.

Ino, T., Doi, T., Hirose, S., Kimura, T., Ito, J., and Fukuyama, H. (2007). Directional disorientation following left retrosplenial hemorrhage: a case report with fMRI studies. Cortex *43*, 248–254.

Ironside, R., and Guttmacher, M. (1929). The corpus callosum and its tumours. Brain *52*, 442–483.

Jiang, X., Shen, S., Cadwell, C.R., Berens, P., Sinz, F., Ecker, A.S., Patel, S., and Tolias, A.S. (2015). Principles of connectivity among morphologically defined cell types in adult neocortex. Science *350*, aac9462.

Katche, C., Dorman, G., Slipczuk, L., Cammarota, M., and Medina, J.H. (2013). Functional integrity of the retrosplenial cortex is essential for rapid consolidation and recall of fear memory. Learn. Mem. *20*, 170–173.

Keene, C.S., and Bucci, D.J. (2008). Contributions of the retrosplenial and posterior parietal cortices to cue-specific and contextual fear conditioning. Behav. Neurosci. *122*, 89–97.

Kim, S.M., Ganguli, S., and Frank, L.M. (2012). Spatial information outflow from the hippocampal circuit: distributed spatial coding and phase precession in the subiculum. J. Neurosci. *32*, 11539–11558.

Koga, K., Li, X., Chen, T., Steenland, H.W., Descalzi, G., and Zhuo, M. (2010). *In vivo* whole-cell patch-clamp recording of sensory synaptic responses of cingulate pyramidal neurons to noxious mechanical stimuli in adult mice. Mol. Pain *6*, 62.

Koike, B.D.V., Farias, K.S., Billwiller, F., Almeida-Filho, D., Libourel, P.-A., Tiran-Cappello, A., Parmentier, R., Blanco, W., Ribeiro, S., Luppi, P.-H., and Queiroz, C.M. (2017). Electrophysiological evidence that the retrosplenial cortex displays a strong and specific activation phased with hippocampal theta during paradoxical (REM) sleep. J. Neurosci. *37*, 8003–8013.

Kurotani, T., Miyashita, T., Wintzer, M., Konishi, T., Sakai, K., Ichinohe, N., and Rockland, K.S. (2013). Pyramidal neurons in the superficial layers of rat retrosplenial cortex exhibit a late-spiking firing property. Brain Struct. Funct. *218*, 239–254.

Lee, S.-H., Marchionni, I., Bezaire, M., Varga, C., Danielson, N., Lovett-Barron, M., Losonczy, A., and Soltesz, I. (2014). Parvalbumin-positive basket cells differentiate among hippocampal pyramidal cells. Neuron *82*, 1129–1144.

Leutgeb, J.K., Leutgeb, S., Moser, M.-B., and Moser, E.I. (2007). Pattern Separation in the Dentate Gyrus and CA3 of the Hippocampus. Science *315*, 961–966.

Liu, P.W., and Bean, B.P. (2014). Kv2 channel regulation of action potential repolarization and firing patterns in superior cervical ganglion neurons and hippocampal CA1 pyramidal neurons. J. Neurosci. *34*, 4991–5002.

Liu, Y.H., and Wang, X.J. (2001). Spike-frequency adaptation of a generalized leaky integrate-and-fire model neuron. J. Comput. Neurosci. *10*, 25–45.

Locke, R.E., and Nerbonne, J.M. (1997). Role of voltage-gated K+ currents in mediating the regular-spiking phenotype of callosal-projecting rat visual cortical neurons. J. Neurophysiol. *78*, 2321–2335.

Maguire, E.A. (2001). The retrosplenial contribution to human navigation: a review of lesion and neuroimaging findings. Scand. J. Psychol. *42*, 225–238.

Mao, D., Kandler, S., McNaughton, B.L., and Bonin, V. (2017). Sparse orthogonal population representation of spatial context in the retrosplenial cortex. Nat. Commun. *8*, 243.

Mao, D., Neumann, A.R., Sun, J., Bonin, V., Mohajerani, M.H., and McNaughton, B.L. (2018). Hippocampus-dependent emergence of spatial sequence coding in retrosplenial cortex. Proc. Natl. Acad. Sci. USA *115*, 8015–8018.

Martina, M., and Jonas, P. (1997). Functional differences in Na+ channel gating between fast-spiking interneurones and principal neurones of rat hippocampus. J. Physiol. *505*, 593–603.

Marx, M., Günter, R.H., Hucko, W., Radnikow, G., and Feldmeyer, D. (2012). Improved biocytin labeling and neuronal 3D reconstruction. Nat. Protoc. *7*, 394–407.

Milczarek, M.M., Vann, S.D., and Sengpiel, F. (2018). Spatial Memory Engram in the Mouse Retrosplenial Cortex. Curr. Biol. *28*, 1975–1980.e6.

Miller, A.M.P., Mau, W., and Smith, D.M. (2019). Retrosplenial Cortical Representations of Space and Future Goal Locations Develop with Learning. Curr. Biol. *29*, 2083–2090.e4.

Miyashita, T., and Rockland, K.S. (2007). GABAergic projections from the hippocampus to the retrosplenial cortex in the rat. Eur. J. Neurosci. *26*, 1193–1204.

Mizuseki, K., Diba, K., Pastalkova, E., and Buzsáki, G. (2011). Hippocampal CA1 pyramidal cells form functionally distinct sublayers. Nat. Neurosci. *14*, 1174–1181.

Murakoshi, H., and Trimmer, J.S. (1999). Identification of the Kv2.1 K+ channel as a major component of the delayed rectifier K+ current in rat hippocampal neurons. J. Neurosci. *19*, 1728–1735.

Nakamura, S., Baratta, M.V., Pomrenze, M.B., Dolzani, S.D., and Cooper, D.C. (2012). High fidelity optogenetic control of individual prefrontal cortical pyramidal neurons *in vivo*. F1000Res. *1*, 7.

Neymotin, S.A., Lazarewicz, M.T., Sherif, M., Contreras, D., Finkel, L.H., and Lytton, W.W. (2011). Ketamine disrupts θ modulation of γ in a computer model of hippocampus. J. Neurosci. *31*, 11733–11743.

Nitz, D.A. (2006). Tracking route progression in the posterior parietal cortex. Neuron *49*, 747–756.

Olson, J.M., Tongprasearth, K., and Nitz, D.A. (2017). Subiculum neurons map the current axis of travel. Nat. Neurosci. *20*, 170–172.

Osawa, A., Maeshima, S., and Kunishio, K. (2007). Topographic disorientation and amnesia due to cerebral hemorrhage in the left retrosplenial region. Eur. Neurol. *59*, 79–82.

Packer, A.M., and Yuste, R. (2011). Dense, unspecific connectivity of neocortical parvalbumin-positive interneurons: a canonical microcircuit for inhibition? J. Neurosci. *31*, 13260–13271.

Page, H.J.I., and Jeffery, K.J. (2018). Landmark-Based Updating of the Head Direction System by Retrosplenial Cortex: A Computational Model. Front. Cell. Neurosci. *12*, 191.

Peyrache, A., and Buzsaki, G. (2015). Extracellular recordings from multi-site silicon probes in the anterior thalamus and subicular formation of freely moving mice. CRCNS – Collaborative Research in Computational Neuroscience. https://doi.org/10.6080/K0G15XS1.

Peyrache, A., Lacroix, M.M., Petersen, P.C., and Buzsáki, G. (2015). Internally organized mechanisms of the head direction sense. Nat. Neurosci. *18*, 569–575.

Rose, M. (1927). Gyrus limbicus anterior and Regio regrosplenialis (Cortex holoprototychos quinquestratificatus): Vergleichende Architektonik bei Tier und Mensch. J. Psychol. Neurol. *35*, 65–173.

Scharfman, H.E. (1992). Differentiation of rat dentate neurons by morphology and electrophysiology in hippocampal slices: granule cells, spiny hilar cells and aspiny "fast-spiking" cells. Epilepsy Res. Suppl. *7*, 93–109.

Scharfman, H.E. (2019). The Dentate Gyrus and Temporal Lobe Epilepsy: An "Exciting" Era. Epilepsy Curr. *19*, 249–255.

Sempere-Ferràndez, A., Andrés-Bayón, B., and Geijo-Barrientos, E. (2018). Callosal responses in a retrosplenial column. Brain Struct. Funct. *223*, 1051–1069.

Sempere-Ferràndez, A., Martínez, S., and Geijo-Barrientos, E. (2019). Synaptic mechanisms underlying the intense firing of neocortical layer 5B pyramidal neurons in response to cortico-cortical inputs. Brain Struct. Funct. *224*, 1403–1416.

Senzai, Y., and Buzsáki, G. (2017). Physiological Properties and Behavioral Correlates of Hippocampal Granule Cells and Mossy Cells. Neuron *93*, 691–704.e5.

Sharp, P.E. (1999). Subicular place cells expand or contract their spatial firing pattern to fit the size of the environment in an open field but not in the presence of barriers: comparison with hippocampal place cells. Behav. Neurosci. *113*, 643–662.

Sharp, P.E., and Green, C. (1994). Spatial correlates of firing patterns of single cells in the subiculum of the freely moving rat. J. Neurosci. *14*, 2339–2356.

Shine, J.P., Valdés-Herrera, J.P., Hegarty, M., and Wolbers, T. (2016). The Human Retrosplenial Cortex and Thalamus Code Head Direction in a Global Reference Frame. J. Neurosci. *36*, 6371–6381.

Sigwald, E.L., Genoud, M.E., Giachero, M., de Olmos, S., Molina, V.A., and Lorenzo, A. (2016). Selective neuronal degeneration in the retrosplenial cortex impairs the recall of contextual fear memory. Brain Struct. Funct. *221*, 1861–1875.

Simonnet, J., and Brecht, M. (2019). Burst Firing and Spatial Coding in Subicular Principal Cells. J. Neurosci. *39*, 3651–3662.

Soltesz, I., and Losonczy, A. (2018). CA1 pyramidal cell diversity enabling parallel information processing in the hippocampus. Nat. Neurosci. *21*, 484–493.

Sterratt, D., Graham, B., Gillies, A., and Willshaw, D. (2011). Principles of Computational Modeling in Neuroscience, First Edition (Cambridge University Press).

Stewart, S., Jeewajee, A., Wills, T.J., Burgess, N., and Lever, C. (2013). Boundary coding in the rat subiculum. Philos. Trans. R. Soc. Lond. B Biol. Sci. *369*, 20120514.

Storm, J.F. (1988). Temporal integration by a slowly inactivating K+ current in hippocampal neurons. Nature *336*, 379–381.

Sudhakar, S.K., Torben-Nielsen, B., and De Schutter, E. (2015). Cerebellar nuclear neurons use time and rate coding to transmit purkinje neuron pauses. PLoS Comput. Biol. *11*, e1004641.

Sudhakar, S.K., Hong, S., Raikov, I., Publio, R., Lang, C., Close, T., Guo, D., Negrello, M., and De Schutter, E. (2017). Spatiotemporal network coding of physiological mossy fiber inputs by the cerebellar granular layer. PLoS Comput. Biol. *13*, e1005754.

Sudhakar, S.K., Choi, T.J., and Ahmed, O.J. (2019). Biophysical Modeling Suggests Optimal Drug Combinations for Improving the Efficacy of GABA Agonists after Traumatic Brain Injuries. J. Neurotrauma *36*, 1632–1645.

Sugar, J., Witter, M.P., van Strien, N.M., and Cappaert, N.L. (2011). The retrosplenial cortex: intrinsic connectivity and connections with the (para)hippocampal region in the rat. An interactive connectome. Front. Neuroinform. *5*, 7.

Takahashi, N., Kawamura, M., Shiota, J., Kasahata, N., and Hirayama, K. (1997). Pure topographic disorientation due to right retrosplenial lesion. Neurology *49*, 464–469.

Taube, J.S. (1995). Head direction cells recorded in the anterior thalamic nuclei of freely moving rats. J. Neurosci. *15*, 70–86.

Taube, J.S., and Bassett, J.P. (2003). Persistent neural activity in head direction cells. Cereb. Cortex *13*, 1162–1172.

Taube, J.S., Muller, R.U., and Ranck, J.B., Jr. (1990). Head-direction cells recorded from the postsubiculum in freely moving rats. I. Description and quantitative analysis. J. Neurosci. *10*, 420–435.

Todd, T.P., and Bucci, D.J. (2015). Retrosplenial Cortex and Long-Term Memory: Molecules to Behavior. Neural Plast. *2015*, 414173.

Todd, T.P., Meyer, H.C., and Bucci, D.J. (2015). Contribution of the retrosplenial cortex to temporal discrimination learning. Hippocampus *25*, 137–141.

Todd, T.P., DeAngeli, N.E., Jiang, M.Y., and Bucci, D.J. (2017). Retrograde amnesia of contextual fear conditioning: Evidence for retrosplenial cortex involvement in configural processing. Behav. Neurosci. *131*, 46–54.

Treves, A. (1993). Mean field analysis of neuronal spike dynamics. Network *4*, 259–284.

Valenstein, E., Bowers, D., Verfaellie, M., Heilman, K.M., Day, A., and Watson, R.T. (1987). Retrosplenial amnesia. Brain *110*, 1631–1646.

Van Groen, T., and Wyss, J.M. (1990). Connections of the retrosplenial granular a cortex in the rat. J. Comp. Neurol. *300*, 593–606.

Van Groen, T., and Wyss, J.M. (2003). Connections of the retrosplenial granular b cortex in the rat. J. Comp. Neurol. *463*, 249–263.

Van Groen, T., Kadish, I., and Wyss, J.M. (2004). Retrosplenial cortex lesions of area Rgb (but not of area Rga) impair spatial learning and memory in the rat. Behav. Brain Res. *154*, 483–491.

Vann, S.D., Kristina Wilton, L.A., Muir, J.L., and Aggleton, J.P. (2003). Testing the importance of the caudal retrosplenial cortex for spatial memory in rats. Behav. Brain Res. *140*, 107–118.

Vann, S.D., Aggleton, J.P., and Maguire, E.A. (2009). What does the retrosplenial cortex do? Nat. Rev. Neurosci. *10*, 792–802.

Vedder, L.C., Miller, A.M.P., Harrison, M.B., and Smith, D.M. (2016). Retrosplenial cortical neurons encode navigational cues, trajectories and reward locations during goal directed navigation. Cereb. Cortex *27*, 3713–3723.

Vierling-Claassen, D., Cardin, J.A., Moore, C.I., and Jones, S.R. (2010). Computational modeling of distinct neocortical oscillations driven by cell-type selective optogenetic drive: separable resonant circuits controlled by low-threshold spiking and fast-spiking interneurons. Front. Hum. Neurosci. *4*, 198.

Wilber, A.A., Clark, B.J., Forster, T.C., Tatsuno, M., and McNaughton, B.L. (2014). Interaction of egocentric and world-centered reference frames in the rat posterior parietal cortex. J. Neurosci. *34*, 5431–5446.

Wu, R.-L., and Barish, M.E. (1992). Two pharmacologically and kinetically distinct transient potassium currents in cultured embryonic mouse hippocampal neurons. J. Neurosci. *12*, 2235–2246.

Wyss, J.M., and Van Groen, T. (1992). Connections between the retrosplenial cortex and the hippocampal formation in the rat: a review. Hippocampus *2*, 1–11.

Wyss, J.M., Van Groen, T., and Sripanidkulchai, K. (1990). Dendritic bundling in layer I of granular retrosplenial cortex: intracellular labeling and selectivity of innervation. J. Comp. Neurol. *295*, 33–42.

Xue, M., Atallah, B.V., and Scanziani, M. (2014). Equalizing excitation-inhibition ratios across visual cortical neurons. Nature *511*, 596–600.

Yamawaki, N., Radulovic, J., and Shepherd, G.M.G. (2016). A corticocortical circuit directly links retrosplenial cortex to M2 in the mouse. J. Neurosci. *36*, 9365–9374.

Yamawaki, N., Corcoran, K.A., Guedea, A.L., Shepherd, G.M.G., and Radulovic, J. (2019a). Differential Contributions of Glutamatergic Hippocampal→Retrosplenial Cortical Projections to the Formation and Persistence of Context Memories. Cereb. Cortex *29*, 2728–2736.

Yamawaki, N., Li, X., Lambot, L., Ren, L.Y., Radulovic, J., and Shepherd, G.M.G. (2019b). Long-range inhibitory intersection of a retrosplenial thalamocortical circuit by apical tuft-targeting CA1 neurons. Nat. Neurosci. *22*, 618–626.

Yoshida, M., and Hasselmo, M.E. (2009). Persistent firing supported by an intrinsic cellular mechanism in a component of the head direction system. J. Neurosci. *29*, 4945–4952.

Yoshimura, Y., and Callaway, E.M. (2005). Fine-scale specificity of cortical networks depends on inhibitory cell type and connectivity. Nat. Neurosci. *8*, 1552–1559.

STAR★METHODS

KEY RESOURCES TABLE

REAGENT or RESOURCE	SOURCE	IDENTIFIER
Chemicals, Peptides, and Recombinant Proteins		
Sodium bicarbonate	Fisher Chemical	Cat#S233
Fluriso	VetOne	Cat#501017
Sodium chloride	Fisher Chemical	Cat#S571
Sodium phosphate monobasic	Sigma	Cat#S5011
Potassium chloride	Fisher Chemical	Cat#P217
Dextrose	Sigma	Cat#D9434
Sucrose	Sigma	Cat#S7903
Calcium chloride dihydrate	Sigma	Cat#C5080
Magnesium sulfate heptahydrate	Sigma	Cat#M5921
D-Gluconic acid solution	Sigma	Cat#G1951
Potassium hydroxide	Sigms	Cat#P5958
HEPES	Sigma	Cat#H3375
EGTA	Sigma	Cat#E3889
GTP sodium salt hydrate	Sigma	Cat#G8877
Phosphocreatine di(tris) salt	Sigma	Cat#P1937
ATP magnesium salt	Sigma	Cat#A9187
Biocytin	Sigma	Cat#B4261
Paraformaldehyde	Acros	Cat#41678
Paraformaldehyde 32% solution	Electron Microscopy Sciences	Cat#15714
Sodium phosphate monobasic monohydrate	Fisher Scientific	Cat#S369
Sodium phosphate dibasic anhydrous	Fisher Scientific	Cat#S375
Vectastain Elite ABC Kit, Peroxidase	Vector laboratories	Cat#PK-6100
SIGMAFAST 3,3′-Diaminobenzidine tablets	Sigma	Cat#D4168
Mowiol	Sigma	Cat#81381
Triton X-100	Sigma	Cat#X100
Streptavidin, Alexa Fluor 488 Conjugate	Thermo Fisher Scientific	Cat#S11223
Streptavidin, Alexa Fluor 594 Conjugate	Thermo Fisher Scientific	Cat#S11227
Streptavidin, Alexa Fluor 647 Conjugate	Thermo Fisher Scientific	Cat#S21374
Fluoromount - G	SouthernBiotech	Cat#0100-01
Experimental Models: Organisms/Strains		
PV-IRES-Cre	Jackson Laboratories	008069; RRID: IMSR_JAX:008069
CaMKII-Cre	Jackson Laboratories	005359; RRID: IMSR_JAX:005359
Ai32	Jackson Laboratories	024109; RRID: IMSR_JAX:024109
Ai14	Jackson Laboratories	007914; RRID: IMSR_JAX:007914
NTSR1-Cre	MMRRC	030648-UCD; RRID: MMRRC_030648-UCD
Software and Algorithms		
NEURON, version 7.5	Hines and Carnevale, 2001	https://neuron.yale.edu/neuron/download
Neurolucida	MBF Bioscience	https://www.mbfbioscience.com/neurolucida
MATLAB, version R2018b	MathWorks	https://www.mathworks.com/downloads/
Clampfit, version 10.6.2.2	Molecular Devices	http://mdc.custhelp.com/app/answers/detail/a_id/18779/~/axon%E2%84%A2pclamp%E2%84%A2-10-electrophysiology-data-acquisition-%26-analysis-software-download

LEAD CONTACT AND MATERIALS AVAILABILITY

Further information and requests for resources and reagents should be directed to and will be fulfilled by the Lead Contact, Dr. Omar J Ahmed (ojahmed@umich.edu). This study did not generate new unique reagents.

EXPERIMENTAL MODEL AND SUBJECT DETAILS

All housing of animals and procedures were approved by the University of Michigan Institutional Animal Care and Use Committee. Multiple mouse lines were used in this study, including PV-IRES-Cre (Jackson Laboratories, 008069), CaMKIIα-Cre (Jackson Laboratories, 005359), Ai32 (Jackson Laboratories, 024109), Ai14 (Jackson Laboratories, 007914), PV-IRES-Cre x Ai14 (crossed in house), PV-IRES-Cre x Ai32 (crossed in house), CaMKIIα-Cre x Ai32 (crossed in house), and NTSR1-Cre (MMRRC, 030648-UCD). All mice excluding the NTSR1-Cre line were on a C57Bl6 background, while the NTSR1-Cre mice had a mixed C57Bl6/ICR background. Mice of both sexes between the ages of P21-31 and P60-65 were included in the experiments.

METHOD DETAILS

Physiological Experimental Methods

Slice preparation

A total of 193 recordings used for intrinsic physiology analyses are included in this study from the following mouse lines: PV-IRES-Cre, CaMKIIα-Cre, Ai32, PV-IRES-Cre x Ai14, PV-IRES-Cre x Ai32, CaMKIIα-Cre x Ai32, and NTSR1-Cre. No differences in cell type properties were observed across mouse lines, while both age and sex were explicitly analyzed in terms of their relationship to cell type properties (see Results).

Mice underwent deep isoflurane anesthesia before decapitation. Brains were removed within one min of decapitation and placed in an ice-cold high-sucrose slicing solution that had been saturated with carbogen gas for at least 30 min prior to use. Coronal slices (300um) were cut using a Leica 1200 VT vibratome. Slices were allowed to rest in the slicing solution for about 2 min before being placed in a carbogen-saturated high-magnesium artificial CSF (ACSF) solution to incubate at body temperature (32°C) for 20 min. The entire bubbling bath was then removed from the heater, allowing the slices to gradually cool to room temperature. Slices rested an additional 30 min at room temperature before use.

Slices were submerged in a recording chamber with a constant flow of ACSF containing 126 mM NaCl, 1.25 mM NaH2PO4, 26 mM NaHCO3, 3 mM KCl, 10 mM dextrose, 1.20 mM CaCl2, and 1 mM MgSO4. Recordings were done between 29-31°C with an ACSF flow rate of 2 mL per min. All recordings were done within 8 h of slicing to ensure reputable health of the cells. Patch pipettes with 2–3 μm diameter and resistances of 3–6 MΩ were filled with a potassium gluconate internal solution containing 130 mM K-gluconate, 2 mM NaCl, 4 mM KCl, 10 mM HEPES, 0.2 mM EGTA, 0.3 mM GTP-Tris, 14 mM phosphocreatine-Tris, and 4 mM ATP-Mg (pH 7.25, ~290 mOsm).

Whole-cell recordings

Slices were visualized using an Olympus BX51WI microscope equipped with Olympus 5x and 60x water immersion lens and the Andor Neo sCMOS camera (Oxford Instruments, Abingdon, Oxfordshire, UK). In most cases, neurons were patched randomly within layers 2/3 of RSG with the exception of experiments in which PV neurons were targeted for patching based on their expression of either an eYFP tag (PV-IRES-Cre x Ai32 cross) or a tdTomato tag (PV-IRES-CRE x Ai14 cross). All recordings were done under current clamp conditions using the Multiclamp 700B and Digidata 1440A (Molecular Devices). Neurons were adjusted for series resistances and held at a resting potential of −65 mV (unless otherwise stated) using a constant holding current injection. Recordings were not corrected posthoc for liquid junction potential. In order to characterize the different neuron types, intrinsic and firing properties of recorded neurons were calculated using the Clampfit and MATLAB software packages.

Synaptic connections between neurons were tested using paired whole-cell recordings. 1 ms current pulses were delivered to the presynaptic neuron at 10 Hz for a total of 1 s (10 pulses). The synaptic responses of the postsynaptic neuron were simultaneously recorded while holding the postsynaptic cell at −55 mV.

Optogenetic testing of CaMKIIα expression

Optogenetic verification of CaMKIIα expression was conducted using CaMKIIα-Cre x Ai32 mice (Jackson Laboratories 005359 and 024109 respectively, crossed in house) in which channelrhodopsin is expressed in CaMKIIα-Cre-expressing neurons. Slices were visualized with the Olympus BX51WI equipped with Olympus 5x and 60x water immersion lens. Expression of channelrhodopsin was marked by fluorescence of the eYFP tag. Neurons were recorded in the same manner as described above with at least one additional protocol to verify functional expression of the channelrhodopsin. One millisecond optogenetic light pulses with a 5,500K white LED (Mightex; maximum power of 14.47 mW measured at the slice focal plane) were delivered at 10 Hz while the neuronal responses were recorded. Direct expression was verified by responses to the light pulses under 0.15 ms.

Morphological investigations with biocytin

Six RS and six LR cells were characterized for their morphology. To determine patched cells' morphology, 5 mg/mL of biocytin was added to the internal solution of recording electrodes. Cells were filled with biocytin (Sigma, cat. no. B4261) throughout the recording session, and the pipette was left attached to the cell for at least 20 min. At the end of the recording, cells were "zapped" with fifteen

1 Hz pulses of 3–4 nA current to improve the diffusion of biocytin into the axon (Jiang et al., 2015). Slices were left to recover in the recording chamber for 30 min before further processing. A detailed description of the biocytin labeling and processing is available elsewhere (Marx et al., 2012). Briefly, slices were filled with biocytin as described above, placed in 4% paraformaldehyde (PFA; Acros Organics, cat no. B0144942) for 12–15 h, and then transferred to phosphate buffer solution (PBS). After 24–48 h in PBS, slices were incubated in avidin-biocytin (ABC Elite kit, VectaShield) for 12 h and then treated with peroxidase to reveal cell morphology. Finally, slices were mounted on microscope slides with Mowiol-based embedding medium and allowed to dry for at least 12 h. Cells were visualized using a Leica DM4000B light microscope equipped with a Leica DMC 6200 CMOS camera.

Morphological investigations with Alexa Fluor

To investigate cell morphology using fluorescence, biocytin (5 mg/mL, Sigma cat no. B4261) was added to the internal solution. Cells were filled with biocytin for a total of 20–30 min each, and the slices were then moved to 4% PFA (Fisher Scientific, cat no. 50-980-494) for overnight incubation. Afterward, slices were washed in PBS, permeabilized in 0.2% Triton-X (Sigma, X-100), and incubated for 48 h in either streptavidin conjugated Alexa Fluor 488, 594, or 647 (1mg/1ml diluted to 1:1000, Thermo Fisher Scientific S11223, S11227, or S21374 respectively). Slices were mounted on glass slides using Fluoromout-G mounting medium (SouthernBiotech, cat no. 0100-01) and glass coverslips and visualized with Leica 6000B microscope equipped with a 10x objective and QImaging Retiga-SRV Fast 1394 camera.

Morphological reconstructions

For morphological analysis, z stacks of filled cells were taken with the Leica SP5 confocal microscope using a 40x dry objective. Reconstructions from z stacks were performed using user-guided mode in Neurolucida software and analyzed in Neurolucida Explorer.

Computational Modeling Methods

Model motivation

Biophysical modeling was utilized to study in detail the computational properties of LR and RS neurons and the possible coding mechanisms by which they could contribute to the spatial navigation functions of the RSC. To this end, we constructed multi-compartmental, biophysically realistic models of the two neuronal subtypes based on anatomical reconstructions and tuned the model parameters so that their intrinsic properties closely match their experimental counterparts. The following section explains in detail the active and passive properties of the LR and RS neuron models. Both LR and RS neuron models will be uploaded to ModelDB (https://modeldb.yale.edu/260192). Unlike the experimental data, where junction potential was not adjusted for, all membrane potential values listed below for the computational model should be considered adjusted for the junction potential.

LR neuron model

Morphology and passive properties

To further elucidate the computational properties of LR neurons, we constructed a biophysically realistic model based on their anatomical reconstruction and physiological properties. The model's morphology (Figure 6E) was imported in NEURON using the import3D tool (Hines and Carnevale, 2001). The model has an input resistance and input capacitance of 384 MΩ and 37.2 pF, respectively, closely matching experimental values of LR neurons. The membrane time constant of the model is 14.29 ms. The resting membrane potential of the model is −77.8 mV.

Both LR and RS neuron models were simulated at a temperature of 30°C, and a q10 value of 3 (Hille, 2001) was used to scale the temperature dependence of ion channel kinetics. The number of segments in each compartment was calculated using the d-lambda rule (Hines and Carnevale, 2001). The axial resistivity for both models is 200 Ω-cm (Vierling-Claassen et al., 2010).

Active properties

Three voltage-gated ion channels were simulated for the LR neuron model: fast sodium current (I_{Na}), delayed rectifier potassium current (I_{Kdr}), and K_v1 current (I_d). In addition, a phenomenological mechanism (I_{adap}) for spike frequency adaptation was modeled (Treves, 1993; Fuhrmann et al., 2002). The properties of these currents are described in detail in the following sections. The LR neuron model has a spike half-width of 0.55 ms and a spike threshold of −53.9 mV. The model exhibits very little spike frequency adaptation, with an adaptation ratio of 1.1, as seen in the experimental data. For both models, the reversal potential of sodium (E_{Na}) and potassium ions (E_K) were set to +50 mV and −96 mV, respectively.

Fast sodium current

The fast sodium current (I_{Na}) responsible for action potential generation was modeled based on Hodgkin Huxley formulation (Hodgkin and Huxley, 1952) using the experimental gating properties of transient sodium current found in RS neurons (Martina and Jonas, 1997). The channel was modeled with 3 activation gates and an inactivation gate. The channel was distributed in all the compartments of the model, and their respective maximal channel conductance (g_{max}) is tabulated in Table S2. The channel equations and parameters (Martina and Jonas, 1997) (voltage dependence of steady state activation/inactivation (m_∞, h_∞), time constants of activation and inactivation gates (τ_m, τ_h), channel current (I_{Na})) is given below.

$$m_\infty = \frac{1}{\left(1 + exp\left(-\left(\frac{v - \theta\_m}{\sigma\_m}\right)\right)\right)} \quad \text{(Equation 1)}$$

$$h_\infty = \frac{1}{\left(1+exp\left(-\left(\frac{v-\theta\_h}{\sigma\_h}\right)\right)\right)} \quad \text{(Equation 2)}$$

$$\tau_m = \left(\left(0.022 + \frac{3.6}{\left(1+exp\left(\frac{(v+27.9)}{7.6}\right)\right)}\right) \times \left(0.009 + \frac{1.9}{\left(1+exp\left(\frac{-(v-1.3)}{12.7}\right)\right)}\right)\right) \quad \text{(Equation 3)}$$

$$\tau_h = \left(0.31 + \frac{14}{\left(1+exp\left(\frac{(v+60)}{12}\right)\right)}\right) \quad \text{(Equation 4)}$$

where $\theta_m = -22.8\,mV, \sigma_m = 11.8\,mV, \theta_h = -62.9\,mV,\ \sigma_h = -10\,mV.$

$$I_{Na} = g_{max} \times m^3 \times h \times (V_m - E_{Na}) \quad \text{(Equation 5)}$$

Delayed rectifier potassium current

Delayed rectifier potassium currents (I_{Kdr}) are known to contribute to action potential repolarization in numerous neuronal subtypes of the brain (Locke and Nerbonne, 1997; Murakoshi and Trimmer, 1999; Guan et al., 2007; Liu and Bean, 2014). We modeled this current in the LR neuron model using the channel gating properties of delayed rectifier potassium currents found in RS neurons (Liu and Bean, 2014). The channel model consists of 2 activation gates (Golomb et al., 2007) and no inactivation gates. The channel's activation time constant (Liu and Bean, 2014) was tuned such that the model's spike half width matches the experimentally obtained values. The channel was distributed in all the compartments of the model, and their g_{max} values are given in Table S2. The equations for voltage dependence of steady state activation (n_∞) and the activation time constant (τ_n) of the channel is described below.

$$n_\infty = \frac{1}{\left(1+exp\left(-\left(\frac{v-\theta\_n}{\sigma\_n}\right)\right)\right)} \quad \text{(Equation 6)}$$

$$\tau_n = \left(\left(0.087 + \frac{3.4}{\left(1+exp\left(\frac{(v+35.6)}{9.6}\right)\right)}\right) \times \left(0.087 + \frac{3.4}{\left(1+exp\left(\frac{-(v-1.3)}{18.7}\right)\right)}\right)\right) \quad \text{(Equation 7)}$$

where $\theta_n = -20\,mV, \sigma_n = 10.4\,mV$

$$I_{Kdr} = g_{max} \times n \times n \times (V_m - E_K) \quad \text{(Equation 8)}$$

K_v1 current

The K_v1 current (also known as the d-current, (I_d)) is a potassium current that is widely known to cause a delay to first action potential in many neuronal subtypes (Storm, 1988; Goldberg et al., 2008; Kurotani et al., 2013). We modeled this current to capture the late spiking property of LR neurons that is observed in our physiological data. The current was modeled using the Hodgkin Huxley formalism (Hodgkin and Huxley, 1952) and based on experimental data (Wu and Barish, 1992) and a previously published model (Golomb et al., 2007) with 3 fast activation gates and a slowly inactivating gate. This channel was distributed only in the somatic compartment of the neuron (Table S2). The voltage dependence of steady state activation/inactivation $(a_\infty,\ b_\infty)$ and their respective time constants (τ_a, τ_b) of the channel are given below.

$$a_\infty = \frac{1}{\left(1+exp\left(-\left(\frac{v-\theta\_a}{\sigma\_a}\right)\right)\right)} \quad \text{(Equation 9)}$$

$$b_\infty = \frac{1}{\left(1+exp\left(-\left(\frac{v-\theta\_b}{\sigma\_b}\right)\right)\right)} \quad \text{(Equation 10)}$$

$$\tau_a = 1.4\,ms, \tau_b = 150\,ms \quad \text{(Equation 11)}$$

where $\theta_a = -50\,mV, \sigma_a = 20\,mV, \theta_b = -70\,mV, \sigma_b = -6\,mV$.

$$I_d = g_{max} \times a^3 \times b \times (V_m - E_K) \quad \text{(Equation 12)}$$

Adaptation current

Spike frequency adaptation was modeled using a linear mechanism (I_{adap}) as described in previous studies (Treves, 1993; Fuhrmann et al., 2002). I_{adap} was modeled using the following equations (Treves, 1993).

$$I_{adap} = g(t) * (V_m - E_K) \quad \text{(Equation 13)}$$

$$\frac{dg}{dt} = -\frac{g}{\tau_g} + g_{adap} \times \delta(t - t_{spike}) \quad \text{(Equation 14)}$$

Briefly, when a cell fires an action potential, $g(t)$ is increased by g_{adap}, which decays to zero with a time constant of τ_g. t_{spike} is the time at which the neuron spikes, and E_K is the potassium reversal potential. $g_{adap} = 10pS$ and $\tau_g = 500ms$ (Liu and Wang, 2001).

RS neuron model

Morphology and passive properties

The RS neuron model in our study is based on the biophysical and anatomical properties of RS neurons in layers 2/3 of RSG. The morphology of the model is based on anatomical reconstructions of its experimental counterpart (Figure 6A). The model's input resistance is 148 MΩ and input capacitance is 96.6 pF. The model has a membrane time constant of 14.29 ms. The model's resting membrane potential is −74.95 mV. Thus, the model's passive properties accurately replicate those of RS neurons in layer 2/3 of RSG. The model's ion channels and active properties are described in detail below.

Active properties

Similar to the LR neuron model, the RS neuron model has 3 voltage gated currents and a current for spike frequency adaptation (I_{adap}). The voltage gated currents incorporated in the RS neuron model are fast sodium current (I_{Na}), delayed rectifier potassium current (I_{Kdr}) and K_v1 current (I_d). The model has a spike half width of 0.92 ms and a spike threshold of −54.12 mV. The spike frequency adaptation ratio of the model is 2.5, closely matching the experimental values.

Fast sodium current

The fast sodium current of the RS neuron model was modeled using Hodgkin Huxley's equations (Hodgkin and Huxley, 1952). The channel's voltage dependence of steady state activation/inactivation and their time constants were modeled using Equations 1, 2, 3, 4, and 5 (Martina and Jonas, 1997). The channel was distributed both in the somatic and dendritic compartments whose g_{max} values are described in Table S2.

Delayed rectifier potassium current

The delayed rectifier potassium current (I_{Kdr}) was modeled based on the channel gating properties of K_v2 currents found in RS neurons (Liu and Bean, 2014). Similar to the LR neuron model, the channel consists of 2 activation gates and does not exhibit any inactivation (Liu and Bean, 2014). Compared to LR neurons, the activation kinetics of I_{Kdr} was slower to account for the larger spike width of RS neurons. The kinetics of this current was chosen to account for the spike width differences between the two neuronal subtypes, as delayed rectifier potassium current plays a vital role in controlling the spike width of many central neurons (Erisir et al., 1999). The channel was placed in the somatic and dendritic compartments of the model (see Table S2 for g_{max} values). The channel equations are given below.

$$n_\infty = \frac{1}{\left(1+exp\left(-\left(\frac{v-\theta\_n}{\sigma\_n}\right)\right)\right)} \quad \text{(Equation 15)}$$

$$\tau_n = \left(\left(0.087 + \frac{9.4}{\left(1+exp\left(\frac{(v+35.6)}{9.6}\right)\right)}\right) \times \left(0.087 + \frac{10.4}{\left(1+exp\left(\frac{-(v-1.3)}{18.7}\right)\right)}\right)\right) \quad \text{(Equation 16)}$$

where $\theta_n = -20\,mV, \sigma_n = 10.4\,mV$

$$I_{Kdr} = g_{max} \times n \times n \times (V_m - E_K) \quad \text{(Equation 17)}$$

K_v1 current

In order capture the observed late spiking behavior of layer 2/3 RS neurons of the RSC, I_d was also modeled in the RS neuron model. The channel's gating mechanisms were modeled using Equations 9, 10, 11, and 12 (Golomb et al., 2007). I_d was distributed only in the somatic compartment of the model (see Table S2 for g_{max} values).

Adaptation current

The spike frequency adaptation in the RS neuron model was modeled using the same schema (I_{adap}) as described for LR neurons (Equations 13 and 14) (Treves, 1993; Fuhrmann et al., 2002). The following parameters were used for this current: $g_{adap} = 800pS$ and $\tau_g = 500\,ms$. In a subset of simulations (Figure 7), the adaptation current in RS cells was explicitly removed to study the contributions of adaptation to RS input-output transformations.

Synaptic inputs

The LR and RS neuron models received background and burst synaptic inputs. 40 AMPA synapses and 40 GABA synapses were uniformly distributed throughout the dendritic tree of both neuron models. Each of the background and burst inputs was randomly assigned to one of the AMPA synapses in the dendritic tree of the LR and RS neuron models. The properties of background and burst inputs are described in detail below. Similarly, each of the background GABAergic inputs discussed below was randomly assigned to one of the GABAergic synapses.

Background inputs

The RS and LR neuron models received 50 AMPAergic background inputs. The time course of synaptic conductance of these background inputs is given by the following equation (Sterratt et al., 2011; Sudhakar et al., 2019),

$$G(t) = g_{max} \times S \times \left[\exp\left(\frac{-t}{\tau_{\text{decay}}}\right) - \exp\left(\frac{-t}{\tau_{\text{rise}}}\right)\right] \quad (18)$$

where τ_{decay} and τ_{rise} represent decay and rise time constant, respectively. g_{max} is the maximal synaptic conductance, and S is a normalization factor that equalizes the maximum of $G(t)$ to g_{max}. The values of τ_{rise} and τ_{decay} were 0.5 ms and 2.5 ms, respectively. The AMPAergic background inputs were modeled as Poisson spike trains with a frequency of 5 Hz and reversal potential of 0 mV (E_{AMPA}).

Similarly, phasic GABAergic inputs (50 inputs) were simulated for both models using Equation 18. The τ_{rise} and τ_{decay} values for these inputs are 0.88 ms and 9.4 ms, respectively (Neymotin et al., 2011). Similar to excitatory background inputs, inhibitory inputs were simulated at a frequency of 5 Hz and reversal potential of −80 mV (E_{GABA}).

The g_{max} values of the excitatory and inhibitory background inputs were chosen to capture the low background firing rates of pyramidal neurons observed *in vivo* and the ratio of excitatory-inhibitory (E-I) synaptic input strength (Xue et al., 2014) of neurons in the superficial layers of the cortex. For the LR neuron model, the g_{max} values of phasic excitatory and inhibitory background inputs were set to 0.2 nS and 1.2 nS, thereby maintaining an E-I ratio seen in experiments (Xue et al., 2014). Similarly, for the RS neuron model, the g_{max} vabib_Peyrache_et_al_2015blues of phasic excitatory and inhibitory background inputs were set to 0.6 nS and 3.6 nS, respectively. The LR and RS neuron models have a background firing rate of ∼1 Hz (Dégenètais et al., 2002; Koga et al., 2010; Nakamura et al., 2012).

Burst inputs

In addition to receiving background synaptic inputs, the models also received synchronous and identical burst inputs of various durations (25 ms, 50 ms, 100 ms, 200 ms, 500 ms, 2000 ms). The LR and RS neuron models received stimulation from 20 synchronous AMPAergic burst inputs. These inputs were jittered over a time period of 2 ms and had a spiking probability which was varied from 0.1 to 1. The jitter and probability were varied across trials. The time course of synaptic conductance of burst inputs were modeled using Equation 18. The τ_{decay} and τ_{rise} of these inputs was set to 0.5 ms and 2.5 ms, respectively. The strength of burst inputs (g_{max}) were set to 1200 pS for both models. For each burst condition (duration), the models were run for 300 trials.

In vivo *dataset related modeling*

In order to determine if LR and RS neuron models can sustain continuous firing as would be expected from the firing of head direction neurons in the preferred direction during motionless conditions, we stimulated the LR and RS neuron models with input spike trains of neurons recorded from the postsubiculum that had one preferred head-direction angle (head-direction cells) of awake mice (Peyrache et al., 2015). Spike data were downloaded from the website of CRCNS (Peyrache and Buzsaki, 2015) and given as input to the neuron models. Briefly, the LR and RS neuron models were stimulated with 20 synchronous input spike trains of head direction

neurons recorded from postsubiculum. Similar to the 200 Hz input simulations, the *in vivo* spikes were also jittered (2 ms) and had a spiking probability that was varied from 0.1 to 1. Simulations were run for one entire awake epoch in the th-1 dataset, 1200 s in duration (Peyrache and Buzsaki, 2015). The simulations were repeated for 30 trials each. SNR was calculated according to Equation 19 below. The resulting SNR was binned and plotted as a function of stimulus duration.

QUANTIFICATION AND STATISTICAL ANALYSIS

Experimental Analysis and Statistics

Neuronal analysis and statistics

From the whole-cell recordings, the following intrinsic neuronal properties were calculated: resting membrane potential, spike threshold, spike amplitude, spike width, input resistance (R_{in}), membrane time constant (τ_m), capacitance (C_{in}), afterhyperpolarization (AHP) amplitude, AHP latency, spike frequency adaptation ratio, latency to first spike, and rheobase. Resting membrane potential was recorded within 2 min of break-in. Cells with severely depolarized break-in potentials (> -55 mV) were not included in this study. Spike threshold, amplitude, width, AHP amplitude, and AHP latency were calculated by averaging all spikes in the first sweep of a 600 ms current step protocol that elicited a firing rate of at least 5 Hz. Spike threshold is calculated from the peak of the third derivative of membrane potential (Cruikshank et al., 2012). Spike amplitude was measured as the voltage change from the spike threshold to the peak of the action potential. Spike width was calculated as the full-width at half-max of the spike amplitude. AHP amplitude was calculated as the voltage change from spike threshold to the peak negativity of the AHP, and AHP latency as the time from peak of the spike to peak negativity of the AHP. Input resistance (R_{in}), membrane time constant (τ_m), and input capacitance (C_{in}) were calculated from a series of small negative current steps ranging from -5 pA to -30 pA, creating a deflection in membrane potential of -2 to -4 mV. R_{in} was calculated using Ohm's law, as the mean voltage change divided by mean current amplitude. τ_m was calculated by fitting a single exponential to the average of the initial 60 ms voltage response, ignoring the first 20 ms. C_{in} was then calculated from those two parameters using the formula $\tau_m = R_{in} \times C_{in}$. Spike frequency adaptation ratio was calculated from the first sweep of the 600ms current step protocol that elicited a firing rate of at least 10Hz (6 spikes per 600ms) using the equation ISI_{last} / ISI_{first}. Rheobase was calculated as the minimum current required to elicit at least one action potential. Latency to first spike and rheobase were each calculated from 1 s current pulses increasing in steps of 1–5 pA. Latency to first spike was calculated as the time from the onset of the rheobase current pulse to the first spike.

To visualize this high-dimensional dataset including 10 normalized electrophysiological properties for each recorded cell (input resistance, input capacitance, membrane time constant, rheobase, adaptation ratio, action potential amplitude, action potential width, action potential threshold, AHP amplitude, and AHP latency), we applied Principal Component Analysis (PCA) to find the most informative dimensions of the data. The loadings of each cell onto the first two principal components were plotted to visualize variation in nearly all properties in a dimensionally reduced space. Cells were grouped into three defined groups (Low Rheobase, Fast Spiking, and Regular Spiking) as confirmed by the existence of distinct clusters in principal component space.

Cells which did not fall under the three defined categories were grouped as "unclassified." This group consists of 10 cells with the following characteristics: 4 cells that had very distinct intrinsic physiology, likely corresponding to other inhibitory subtypes, 3 cells with uncharacteristically broad spike widths >1.6 ms, 2 cells with hybrid LR-like and RS-like characteristics, and 1 cell with FS-like characteristics but with surprisingly broad action potentials.

A two-tailed Wilcoxon rank sum test was used to compute the statistical significance between the intrinsic properties of various neuronal subtypes. To establish the statistical significance between the probability of E→I and I→E connections, a bootstrap resampling (1000 bootstrap samples) method was used to generate a distribution of connectivity probabilities (Sudhakar et al., 2017). Briefly, a connectivity matrix was generated which consists of a pre-synaptic label (E or I), post-synaptic label (E or I), and an observation (0 or 1) saying whether the pair is connected. This matrix was bootstrapped (n = 1000), and a distribution of E→I and I→E connectivity probabilities was thus formed. Statistical significance was computed using a two-tailed t test (Henseler et al., 2009) with a confidence interval of 95%. Significance in the number of LR neurons in layer 2/3 versus layer 5/6 was established by Pearson chi-square test (Agresti, 2007). The same statistical test was used to establish whether the proportion of LR neurons in layer 2/3 was significantly different from that of RS neurons.

Connectivity analysis and statistics

When analyzing connected pairs, latency to onset of an IPSP or EPSP was calculated as the time from the peak of the presynaptic action potential to the onset of the postsynaptic IPSP or EPSP. Latency to peak was calculated as the time from the peak of the presynaptic action potential to the peak of the postsynaptic IPSP or EPSP.

To test if the connectivity between different neuronal populations are significantly different from chance, we randomly shuffled the pre-synaptic, post-synaptic labels and the observation (whether the pair is connected) for 1000 trials. By doing this, we established the distribution of chance probabilities for each connectivity pair. We then utilized one-sample t test (two-tailed, 95% confidence interval) to determine if the experimentally observed connectivity probabilities differed significantly from their chance distributions.

Morphological analysis and statistics

For morphological comparisons, cell body surface, number and length of dendrites, and Sholl analysis (at 10 μm intervals) were extracted directly from Neuron Summary, Sholl – dendrites, and Sholl – apical dendrites analysis results in Neurolucida Explorer. Apical

and basal dendrites were added together for all calculations, and data were plotted in MATLAB using custom scripts. Statistical differences were calculated using a two-tailed Wilcoxon rank sum test for all morphological comparisons.

Computational Analysis and Statistics

The models were simulated using NEURON 7.5 simulation environment (Hines and Carnevale, 2001) with an integration time step of 0.025 ms. Simulation output was written into binary files and analyzed using custom programs written in MATLAB (R2018b) software. Spike threshold, spike half width, input resistance, membrane time constant, and input capacitance of the models were calculated using the same method that was used for experimental data.

Signal to noise ratio (SNR) in response to the burst input was computed by calculating the number of spikes in response to the burst input and comparing it with the background response for the same duration as the burst response. SNR in our study is calculated using the following formula (Duguid et al., 2012),

$$SNR = \frac{S_{burst} - S_{back}}{\sqrt{0.5 \times (Var_{burst} + Var_{back})}} \quad \text{(Equation 19)}$$

S_{burst} is the average number of spikes in 'x' ms post burst onset, where x = burst duration+125 ms. S_{back} is the average number spikes per 'x' ms from 4000 ms to 8000 ms post burst onset. Var_{burst} and Var_{back} are the corresponding variances of the number of spikes during those two time intervals.

The spike timing precision (jitter) in response to the burst input was computed by calculating the median absolute deviation of spike latencies from all trials. Bootstrapped resampling was then used to compute a distribution of jitter values, and significance between the jitter of LR and RS neurons was established by 2-tailed t test (95% confidence interval) (Sudhakar et al., 2015). Significance in the probability of spiking between LR and RS neurons was established by Pearson chi-square test (Agresti, 2007) (95% confidence interval).

For simulations related to Figure S4, location dependence of different synaptic inputs along the dendritic tree of LR and RS neuron models was eliminated using the following equation,

$$g_{max_{scaled}} = g_{max} + (g_{max} * dist * m) \quad \text{(Equation 20)}$$

where the value of g_{max} is 1200 pS as mentioned before, and 'dist' is the Euclidean distance between the location of the synaptic input on the dendritic tree and the model's somatic location. The scaling factor, 'm,' was tuned until the location dependence of synaptic input was removed/normalized.

DATA AND CODE AVAILABILITY

The NEURON models/code describing the LR and RS neuron models used in this study have been uploaded to ModelDB (https://modeldb.yale.edu/260192). The experimental datasets generated in this study are available upon reasonable request to the corresponding author.

Cell Reports, Volume *30*

Supplemental Information

Hyperexcitable Neurons Enable Precise and Persistent Information Encoding in the Superficial Retrosplenial Cortex

Ellen K.W. Brennan, Shyam Kumar Sudhakar, Izabela Jedrasiak-Cape, Tibin T. John, and Omar J. Ahmed

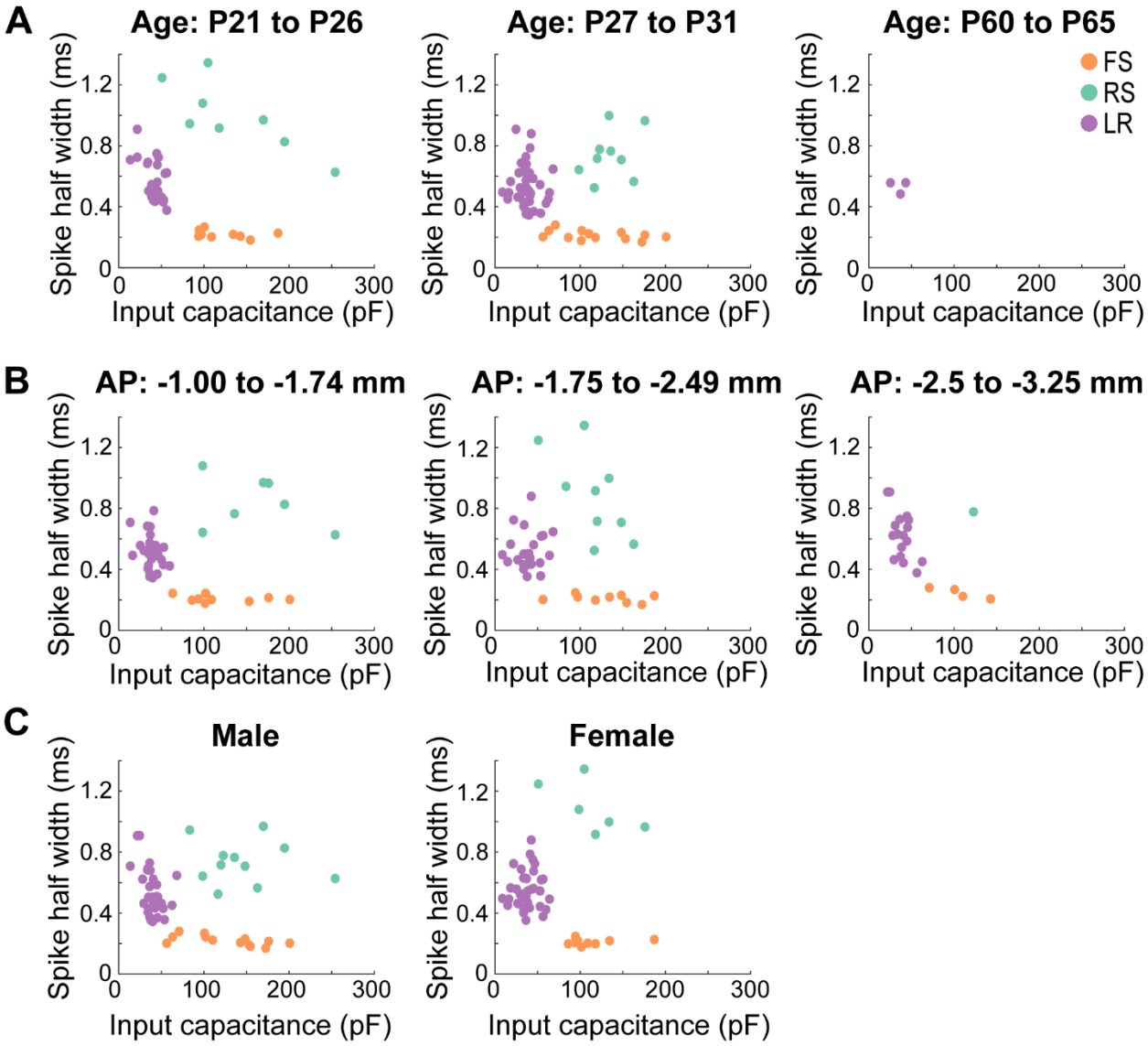

Figure S1. Low Rheobase cells are consistent across age, sex, and long-axis of the RSG. Related to Figure 1 and Table 1.

A. Scatterplots of the three cell types plotted as a function of spike width and input capacitance across different age groups. Left panel, Postnatal days 21-26 (FS: *n* = 9; RS: *n* = 8; LR: *n* = 24). Middle panel, Postnatal days 27-31 (FS: *n* = 13; RS: *n* = 9; LR: *n* = 45). Right panel, Postnatal days 60-65 (LR: *n* = 3).
B. Similar to ***A***, now plotted across distinct anterior-posterior sections of the RSG. Left panel, -1 to -1.74 mm from bregma (FS: *n* = 9; RS: *n* = 7; LR: *n* = 29). Middle panel, -1.75 to -2.49 mm from bregma (FS: *n* = 9; RS: *n* = 9; LR: *n* = 26). Right panel, -2.5 to -3.25 mm from bregma (FS: *n* = 4; RS: *n* = 1; LR: *n* = 17).
C. Similar to ***A***, but now plotted across sex. All three cell types exist and cluster consistently in both male (FS: *n* = 13; RS: *n* = 11; LR: *n* = 34) and female (FS: *n* = 9; RS: *n* = 6; LR: *n* = 38) mice.
Cell numbers in each panel reflect neurons which had both the 600 ms current steps protocol and small negative current steps protocol run (see Methods).

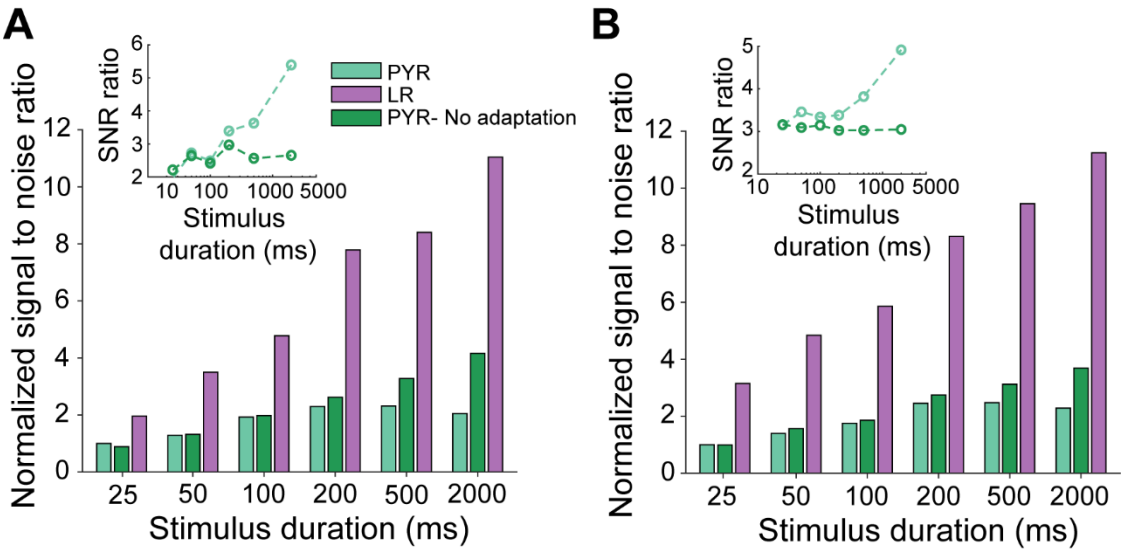

Figure S2. SNR of the RS and LR neuron models to inputs of various durations when the background firing frequency is increased to 10 and 20 Hz. Related to Figure 7.

A. SNR of the RS and LR neuron models to 200 Hz input of varying durations when background firing frequency is 10 Hz.

B. Same as ***A*** with background firing frequency increased to 20 Hz.

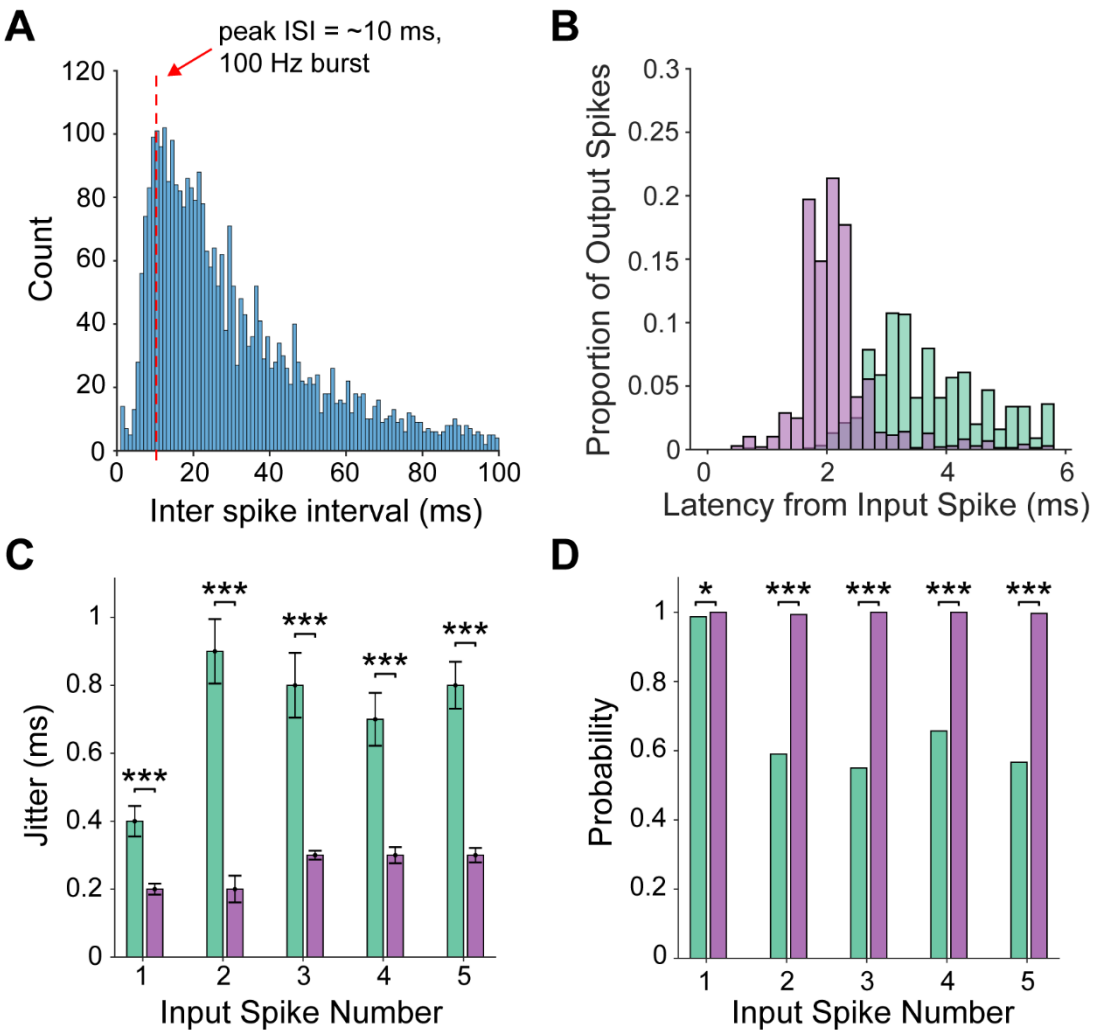

Figure S3. Response of the RS and LR neuron models to *in vivo* like spike trains. Related to Figure 7.

A. ISI distribution of *in vivo* spike trains showing peak firing rate at ~100 Hz.

B. Distribution of spike latencies of the RS and LR neuron models when stimulated with 100 Hz spike trains for 2 seconds.

C. Spike timing precision of the RS and LR neuron models in response to each spike of the burst input (*** p<0.001; two-tailed t-test).

D. Spike probability of the two models to each individual spike within the burst input (*** p<0.001, * p<0.05; Pearson chi-square test).

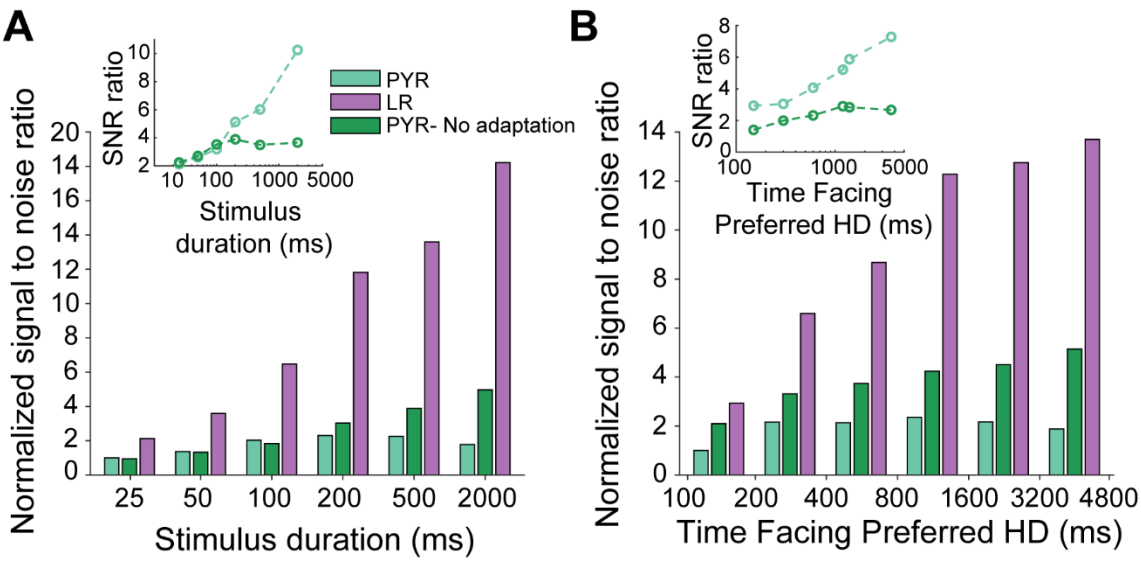

Figure S4. SNR of the RS and LR neuron models when location dependence of dendritic synaptic inputs was removed. Related to Figure 7.

A. SNR of the RS and LR neuron models in response to 200 Hz burst input of varying durations. Synaptic inputs were normalized to get rid of the dendritic location dependence. LR neurons have superior SNR compared to RS neurons. The difference in SNR increases with stimulus duration due to the spike frequency adaptation of RS neurons (inset).

B. Same as ***A***, when both RS and LR neuron models were stimulated with realistic *in vivo* spike trains from the postsubiculum head-direction cell as shown in Fig. 7I. Therefore, even when dendritic location dependence of synaptic inputs was eliminated, the LR neuron model is characterized by superior SNR compared to the RS neuron model.

Category	P21-P26 *(n)*	P27-P31 *(n)*	P60-P65 *(n)*	AP -1 to -1.74 *(n)*	AP -1.75 to -2.49 *(n)*	AP -2.5 to -3.25 *(n)*	Male *(n)*	Female *(n)*
Input resistance (MΩ)	384.90 ± 25.61 *(33)*	416.01 ± 21.45 *(47)*	380.20 ± 52.80 *(3)*	397.06 ± 19.27 *(35)*	410.01 ± 31.99 *(30)*	399.85 ± 35.66 *(18)*	397.38 ± 22.92 *(38)*	406.54 ± 22.29 *(45)*
Input capacitance (pF)	41.28 ± 1.87 *(33)*	36.73 ± 1.89 *(47)*	35.07 ± 5.31 *(3)*	38.99 ± 1.64 *(35)*	38.96 ± 2.50 *(30)*	36.68 ± 3.27 *(18)*	39.65 ± 2.02 *(38)*	37.49 ± 1.76 *(45)*
Action potential width (ms)	0.60 ± 0.04 *(35)*	0.52 ± 0.02 *(62)*	0.53 ± 0.02 *(3)*	0.53 ± 0.02 *(44)*	0.54 ± 0.04 *(32)*	0.62 ± 0.03 *(24)*	0.55 ± 0.02 *(51)*	0.56 ± 0.03 *(49)*
Spike frequency adaptation ratio	1.42 ± 0.12 *(35)*	1.19 ± 0.04 *(62)*	0.99 ± 0.17 *(3)*	1.18 ± 0.04 *(44)*	1.25 ± 0.08 *(32)*	1.44 ± 0.18 *(24)*	1.24 ± 0.05 *(51)*	1.29 ± 0.09 *(49)*
Rheobase (pA)	39.40 ± 2.68 *(42)*	41.68 ± 3.36 *(36)*	40.44 ± 15.11 *(2)*	37.64 ± 2.79 *(39)*	40.62 ± 4.12 *(26)*	46.84 ± 4.21 *(16)*	41.84 ± 2.52 *(43)*	38.84 ± 3.41 *(37)*

Table S1. Low Rheobase (LR) neuron properties are consistent across age, AP, and sex. Related to Figure 1, Table 1, and Figure S1.
Key intrinsic properties calculated for LR neurons grouped by age, AP, and sex.

	RS neuron model	RS neuron model	LR neuron model	LR neuron model
Parameter Description	**Soma**	**Dendrites**	**Soma**	**Dendrites**
Specific membrane resistance ($k\Omega cm^2$)	14.29	14.29	14.29	14.29
Specific membrane capacitance ($\mu F/cm^2$)	1	1	1	1
Membrane time constant	14.29	14.29	14.29	14.29
Axial resistivity (Ω-cm)	200	200	200	200
I_{Na} g_{max} (S/cm^2)	2	0.5	5.5	0.81
I_{Kdr} g_{max} (S/cm^2)	0.02	0.008	0.07	0.006
I_d g_{max} (S/cm^2)	0.0125	0	0.075	0
I_{adap}, g_{adap} (pS)	600	0	10	0

Table S2. Model parameters. Related to Figures 6 & 7 and STAR Methods.
The table lists the values of various model parameters and distribution of ion channel conductances in the somatic and dendritic compartments of the LR and RS neuron models.